Characterization of radiolytically synthesized feroxyhyte and magnetite nanoparticles

Ivan Marić[1], Goran Dražić[2], Goran Štefanić[3,4], Krešo Zadro[5], Marijan Gotić[3,4,*], Tanja Jurkin[1,*]

[1]*Radiation Chemistry and Dosimetry Laboratory, Ruđer Bošković Institute, Bijenička c. 54, 10000 Zagreb, Croatia*

[2]*Department of Materials Chemistry, National Institute of Chemistry, Hajdrihova 19, SI-1001 Ljubljana, Slovenia*

[3]*Center of Excellence for Advanced Materials and Sensing Devices, Ruđer Bošković Institute, Bijenička c. 54, 10000 Zagreb, Croatia*

[4]*Laboratory for Molecular Physics and Synthesis of New Materials, Division of Materials Physics, Ruđer Bošković Institute, Bijenička c. 54, 10000 Zagreb, Croatia*

[5]*Physics Department, Faculty of Science, University of Zagreb, Bijenička c. 32, HR-10000 Zagreb, Croatia*

Abstract

Iron(III) chloride deaerated alkaline aqueous colloidal solutions in the presence of 2-propanol and DEAE-dextran (diethylaminoethyl-dextran hydrochloride) were γ-irradiated with doses of 36 and 130 kGy. The dose rates were ~7 and ~31 kGy h^{-1}. Substoichiometric $Fe_{2.83}O_4$ magnetite nanoparticles ~4.7 nm in size were formed at a dose rate of ~7 kGy h^{-1} and at a dose of 36 kGy. At a dose of 130 kGy the anisotropic δ-FeOOH magnetic discs with a diameter of ~256 nm and thickness of ~40 nm self-assembled. Each disc has a substructure consisting of approximately eighteen laterally stacked thin nanodiscs of about 2.2 nm in thickness. At a higher dose rate of ~31 kGy $h^{-1}$and at a dose of 36 kGy, XRD revealed the presence of substoichiometric $Fe_{2.75}O_4$ magnetite, whereas TEM analysis revealed the presence of ~4.3 nm magnetite nanoparticles along with rod-shaped γ-Fe_2O_3 nanoparticles. At a higher dose rate and at dose of 130 kGy, the rolled rod-like δ-FeOOH magnetic nanoparticles were formed having the diffraction patterns with streaks, which are characteristic of tubular structures. The magnetic measurements showed exceptional intrinsic room-temperature magnetic properties of both δ-FeOOH nanostructures with the Curie temperature above 300 K. In order to ascertain the formation of Fe(II) intermediate products prior to their oxidation, γ-irradiated samples were isolated by admixing glycerol. The amounts of Fe(II) in glycerol-isolated solid samples were 9.9 % and 86.0 %, as determined by Mössbauer spectroscopy at doses of 36 and 130 kGy, respectively. Carbonate Green Rust I, GR(CO_3^{2-}), and $Fe(OH)_2$ intermediate phases were confirmed by XRD and Mössbauer spectroscopy. The amounts of Fe^{2+} in the acidified solutions containing dissolved γ-irradiation products were determined using the potassium permanganate titration. The amounts of Fe^{2+} were 68.9% and 96.1% at doses of 36 and 130 kGy, respectively. Thus, at a dose of 130 kGy the radiolytically generated $Fe(OH)_2$, after coming in contact with oxygen and CO_2 from the air, topotactically oxidized to GR(CO_3^{2-}) and further to δ-FeOOH without any structural changes. The lower dose rate (~7 kGy h^{-1}) favored the δ-FeOOH nanodisc morphology, whereas the higher dose rate (~31 kGy h^{-1}) favored the formation of tubular rod-like δ-FeOOH nanoparticles.

Keywords: gamma-irradiation; amino dextran; green rust; iron(II) hydroxide; feroxyhyte; magnetite

*Corresponding authors: Tanja Jurkin, Ruđer Bošković Institute, Bijenička 54, 10000 Zagreb, Croatia, Phone: +385 1 4571 255, *E-mail address*: tjurkin@irb.hr and Marijan Gotić, Ruđer Bošković Institute, Bijenička 54, 10000 Zagreb, Croatia, *E-mail address*: gotic@irb.hr

1. Introduction

Magnetic nanoparticles (NPs) have been used as contrast agents for magnetic resonance imaging, as drug carriers for controlled drug release and as therapeutic agents for hyperthermia based cancer treatments [1,2]. Along with biocompatibility and non-toxicity, the stability of magnetic NPs in aqueous solutions is of utmost importance [3–6]. Magnetic NPs with sizes up to ~10 nm show superparamagnetic behavior, i.e. their magnetization is zero in the absence of an external magnetic field. The lack of remanent magnetization after removal of external field enables the superparamagnetic NPs to maintain their colloidal stability and to avoid aggregation in aqueous solutions. The larger-sized magnetic NPs out of the superparamagnetic range have a strong tendency to aggregate and therefore, their stabilization in aqueous solutions is still a challenge. Small organic molecules, surfactants, polymers and/or biomolecules can be used as protective agents in order to ensure high stability of magnetic NPs in aqueous solutions.

The radiolytic (γ-irradiation) approach is a non-conventional synthetic route for obtaining magnetic NPs of controlled size, shape and phase composition [7–15]. It takes advantage of high-energy γ-radiation (1.25 MeV for ^{60}Co γ-rays) that is able to ionize an aqueous phase. γ-irradiation of aqueous solutions generates a variety of species such as free radicals (e_{eq}^-, $H^\bullet$, $^\bullet OH$, $HO_2^\bullet$) and molecular products (H_2, H_2O_2), mainly products of water radiolysis. Hydrated electron e_{aq}^-, is a strong reducing agent that is able to reduce metal cations such as Fe^{3+} in an

aqueous solution. Therefore, γ-irradiation can be used as a non-conventional synthetic route for obtaining magnetite (Fe_3O_4) NPs. For instance, Wang et al. [8] have reported the γ-irradiation synthesis of magnetite NPs starting from β-FeOOH alkaline aqueous suspension. In our previous work [11], the substoichiometric magnetite ($Fe_{3-x}O_4$) NPs were synthesized using γ-irradiation of water-in-oil microemulsions containing Fe(III). The stoichiometry of thus synthesized magnetite NPs depended on the absorbed dose and dose rate.

The radiolytic synthesis of δ-FeOOH magnetic NPs is being much less investigated [12,14,15]. δ-FeOOH is a synthetic analog of a relatively uncommon mineral feroxyhyte (δ'-FeOOH). For simplicity, in this work, the δ-FeOOH has been equated with the mineral feroxyhyte. δ-FeOOH possesses specific structural and magnetic properties and unlike all the other iron oxyhydroxide polymorphs (α-FeOOH – antiferromagnetic; β-FeOOH and γ-FeOOH - paramagnetic), it is magnetic at room temperature [16–19]. The magnetic properties of feroxyhyte depend critically on the crystallite and/or particle size [19]. Pollard and Pankhurst [20] have reported that the feroxyhyte (feroxyhite) behavior is consistent with ferrimagnetism. Koch et al. [18] regarded a well-crystallized feroxyhyte as a planar antiferromagnet with magnetic moments along the *c*-axis. A net magnetization in such material arose due to the very small number of layers along the *c*-direction, thus causing the formation of ferromagnetic domains and due to the presence of spins randomly canted away from the *c*-axis.

δ-FeOOH structure is based on a hexagonal close-packed (hcp) oxygen lattice similar to that of hematite (α-Fe_2O_3) with iron ions distributed over octahedral and tetrahedral sites or over two octahedral sites [21]. The oxygen anions are partly replaced by OH and OH_2 and the degree of occupancy of Fe is less than 2/3 similar as it is in hematite. Moreover, Pereira et al. [22] pointed out that δ-FeOOH is always associated with finely dispersed hematite. On the other hand, Sestu et al. [23] proposed the structure for δ-FeOOH that is based on the structure of the thermodynamically stable iron oxyhydroxide goethite (α-FeOOH).

δ-FeOOH has been used in various applications [22,24,25], such as a photocatalyst or for arsenic removal from contaminated water. Pereira et al. [22] have reported on the first use of nanostructured δ-FeOOH, with the band gap energy in the visible region, as a promising photocatalyst for the production of hydrogen from water. Pinto et al. [26] have used δ-FeOOH as a heterogeneous catalyst in order to stimulate the degradation of organic contaminants such as a cationic (methylene blue) and an anionic dye (indigo carmine). It has been shown that δ-

FeOOH can activate H_2O_2 to produce reactive radicals, which then further promote the degradation of the dyes. Recently, the synthesis of δ-FeOOH ultrathin nanosheet as a new 2D inorganic graphene-like material that exhibited a high saturation magnetization of 7.5 emu g^{-1} at room temperature has been reported [27]. The δ-FeOOH ultrathin nanosheet was found to be a semiconductor with a direct band gap of 2.2 eV. Chagas et al. reported [28] that δ-FeOOH released a controlled amount of heat if placed under the AC magnetic field, which classified δ-FeOOH as a promising material for biomedical applications. Martins et al. [29] have reported that magnetic δ-FeOOH nanosheets embedded in a poly[vinylidenefluoride-co-trifluoroethylene] P(VDF-TrFE) piezoelectric matrix show anisotropic magnetoelectric response that is able to detect the magnetic field amplitude and direction. Liu et al. [30] synthesized ultrathin δ-FeOOH nanosheets with rich Fe vacancies on a Ni foam substrate. The formation of rich second neighboring Fe to Fe vacancies in δ-FeOOH nanosheets created catalytic active centers for both hydrogen and oxygen evolution reactions, thus enabling efficient overall water splitting.

δ-FeOOH can be formed by the atmospheric corrosion of steel and/or by electrochemical cycling of nanostructured hematite in alkali aqueous solutions. The conventional syntheses of δ-FeOOH start from a Fe(II) salt and proceed by rapid oxidation of iron(II) hydroxide with H_2O_2. Gotić et al. [31] have reported that strong alkalinity of the mother liquor was an important factor for δ-FeOOH formation via the $Fe(OH)_2$ precursor. Besides, it has been found that a small amount of Fe^{3+} ions present in the $Fe(OH)_2$ precursor before the rapid oxidation of Fe^{2+} ions with H_2O_2, was not critical for the formation of δ-FeOOH as a single phase. Olowe et al. [32] showed that δ-FeOOH could be obtained by oxidation of an intermediate phase “Green rust I” that was formed by the precipitation of $Fe(OH)_2$ in an excess of OH^- ions. Polyakov et al. [33] have reported the synthesis of anisotropic magnetic δ-FeOOH nanoparticles in the presence of humic substances (natural polyelectrolytes). It has been shown that humic substances highly reduced the δ-FeOOH mean size and enhanced its colloidal stability in salt solutions. Nishida et al. [34] synthesized superparamagnetic (10 nm in diameter) spherical δ-FeOOH NPs that showed increased magnetization intensity relative to that of bulk δ-FeOOH. It was found that δ-FeOOH NPs formed by oxidation of Fe_3O_4 and $Fe(OH)_2$ intermediate products.

In our previous works [12,15] the impact of various polymers and surfactants such as poly(ethylene oxide) (PEO), polyvinylpyrrolidone (PVP), cetyl trimethylammonium bromide

(CTAB) and diethylaminoethyl-dextran hydrochloride (DEAE-dextran) on the γ-irradiation synthesis of iron oxides has been studied. It has been shown that a small amount of δ-FeOOH formed upon γ-irradiation of deoxygenated $FeCl_3$ alkaline aqueous suspension in the presence of CTAB and PVP. γ-irradiation of deoxygenated $FeCl_3$ alkaline aqueous suspension in the presence of DEAE-dextran has yielded even better results, because for the first time δ-FeOOH magnetic nanodiscs were obtained as an end product. The synthesis of δ-FeOOH nanodiscs using γ-irradiation is quite surprising, because δ-FeOOH has never been synthesized; *(i)* starting from Fe(III) precursor, *(ii)* using γ-irradiation and *(iii)* in nanodisc morphology. δ-FeOOH as a rule consists of irregular, plate-like morphology. In a previous paper [15] we have hypothesized that γ-irradiation generated highly reducing conditions that reduced the Fe(III) precursor to Fe(II) intermediate products. Actually, we have observed that the white suspension characteristic of $Fe(OH)_2$ was formed, which after coming in contact with the air turned to a green-gray suspension characteristic of Green Rust. These Fe(II) intermediate products are extremely susceptible to oxidation and they have not been experimentally confirmed in previous work [15].

In continuation with our previous work [14,15], herein we present new results regarding the synthesis and microstructural characterization of radiolytically synthesized δ-FeOOH and substoichiometric magnetite ($Fe_{3-x}O_4$) NPs. The highly reactive Fe(II) intermediate phases, namely $Fe(OH)_2$ and carbonate Green Rust I ($GR(CO_3^{2-})$), were isolated by admixing glycerol and characterized using XRD and Mössbauer spectroscopy. The concentrations of ferrous ions (Fe^{2+}) in acidified solutions containing dissolved γ-irradiation products were determined using $KMnO_4$ titration. The electron microscopy analysis of radiolytically synthesized samples demonstrated the unique nanodisc and tubular rod-like δ-FeOOH morphologies.

2. Materials and methods

2.1. Chemicals

All chemicals were of analytical purity and used as received. Milli-Q deionized water was used. Iron(III) chloride hexahydrate ($FeCl_3 \bullet 6H_2O$), sodium hydroxide (NaOH) and 2-propanol ($(CH_3)_2CHOH$)) were supplied by Kemika, Zagreb. Diethylaminoethyl dextran

hydrochloride (DEAE-dextran) prepared from dextran of average molecular weight 500,000 was produced by *Sigma*.

2.2. Synthesis of δ-FeOOH nanoparticles

Firstly, the 2M $FeCl_3$ and 1.85 wt% DEAE-dextran hydrochloride aqueous stock solutions were prepared. Then, 176 μL (0.35 mmol) of 2 M $FeCl_3$ and 308 μL (4.00 mmol) of 2-propanol were added to 20 mL of 1.85 wt% DEAE-dextran hydrochloride aqueous solution. The pH of thus prepared solution was adjusted to ~9 by adding 2 M NaOH aqueous solution. The solutions were bubbled for 30 minutes with nitrogen in order to remove the dissolved oxygen (deaerated solution) and then γ-irradiated (without stirring) in a closed glass vial using panoramic ^{60}Co source at Radiation Chemistry and Dosimetry Laboratory at the Ruđer Bošković Institute. The dose rates of γ-irradiation were ~7 or 31 kGy h^{-1}. The absorbed doses were 36 and 130 kGy. The redish-brown-orange solution upon γ-irradiation at 36 kGy turned to stable brown-black solution, whereas upon γ-irradiation at 130 kGy the white suspension were formed, which after opening the glass vial turned to green suspension. The samples were isolated by washing with ethanol and centrifugation using ScanSpeed 2236R high-speed centrifuge. The isolated precipitates were dried under vacuum at room temperature and then characterized as powder samples. Samples named as S1 and S2 were irradiated at a lower dose rate of ~7 kGy h^{-1} with 36 kGy and 130 kGy, respectively. Samples named as S3 and S4 were irradiated at a higher dose rate of 31 kGy h^{-1} with 36 kGy and 130 kGy dose, respectively.

2.3. Determination of Fe^{2+} in γ-irradiated suspensions by potassium permanganate titration

2.3.1. Chemicals for permanganate titration

Potassium permanganate solution (0.02 M, standardized against oxalate) supplied by *Merck*, hydrochloric acid (fuming, ≥37 wt%) by *Fluka;* manganese(II) sulfate monohydrate (p.a. EMSURE, ACS, reag. Ph. Eur.) by *Merck*, orthophosphoric acid (85% p.a.) by *LachNer*, sulfuric acid (96%, p.a.) by *LachNer*, tin(II) chloride dehydrate (p.a., EMSURE, ACS, ISO, Reag. Ph. Eur.) by *Merck* and mercury(II) chloride (analytical reagent grade) supplied by *Fisher Scientific* were used.

2.3.2. Potassium permanganate titration

In order to determine the Fe^{2+} concentration in γ-irradiated suspensions, the permanganate titration procedure was performed. Immediately after irradiation, concentrated

hydrochloric acid (2.5 mL of 37 wt% HCl solution) was added by syringe through rubber septa to 100 mL of γ-irradiated suspensions in order to dissolve all formed precipitates and lower the pH to slightly below 1. At such low pH, a clear solution formed that preserved all Fe^{2+} formed upon γ-irradiation. Furthermore, at such low pH, the Fe^{2+} ions are not able to oxidize to Fe^{3+}. Then, the γ-irradiated solutions were titrated with 0.02 M potassium permanganate solution following the standard permanganate titration procedure (with the addition of Zimmermann-Reinhardt solution). The Fe^{2+} concentration formed on γ-irradiation were determined, as well as total iron concentration. To check the total iron concentration, the remaining Fe^{3+} (not reduced by γ-irradiation) was reduced with tin(II) chloride, and a small excess of $SnCl_2$ was treated with mercury(II) chloride prior to titration.

2.4. Characterization of samples

The morphology of samples was investigated using a probe Cs-corrected cold field-emission Scanning Transmission Electron Microscope (STEM), model ARM 200 CF, and the thermal field emission scanning electron microscope (FE SEM, model JSM-7000 F) manufactured by JEOL Ltd. FE SEM was linked to the EDS/INCA 350 (energy-dispersive X-ray analyzer) manufactured by Oxford Instruments Ltd.

X-ray powder diffraction (XRD) patterns were recorded at 20 ^{o}C using an APD 2000 X-ray powder diffractometer (Cu *K*α radiation) manufactured by ItalStructures. The XRD patterns were recorded over a 5–80 2θ range with 2θ step of 0.025 ^{o} and accounting time per step of 20 – 33 s. The samples were put on XRD Si zero-background holder in the form of a thin layer. Silicon (*Koch-Light Lab. Ltd.*) was used as an internal standard for precise lattice parameter determinations. The diffraction patterns were fitted using GSAS software [35]. Le Bail method [36] for whole-pattern fitting was used and the profile function used was the Thompson-Cox-Hastings pseudo-Voigt function.

^{57}Fe Mössbauer spectra were recorded at 20 ^{o}C in the transmission mode using a standard instrumental configuration by Wissel GmbH (Starnberg, Germany). ^{57}Co in a rhodium matrix was used as a Mössbauer source. The spectrometer was calibrated at 20 °C using the standard α-Fe foil spectrum. The velocity scale and all the data refer to the metallic α-Fe absorber at 20 °C. The experimentally observed Mössbauer spectra were fitted using the MossWinn program.

The magnetic properties of the nanoparticles were measured using a Superconducting Quantum Interference Device (SQUID) magnetometer, model MPMS-5 furnished with a

superconducting magnet producing fields up to 5.5 T. The powder samples were put into a small plastic capsule, sealed with silicon paste, weighed, and then properly closed. The magnetic measurements started by cooling down the sample to 20 K from room temperature in zero applied field (H = 0) [37]. Once stabilized, a magnetic field was applied (H = 100 Oe) and the variation of the magnetic moment of the sample was measured during the increase of temperature (T) up to 300 K. This gave zero-field-cooled (ZFC) curve. Subsequently, the sample was cooled to 20 K in the same applied magnetic field of 100 Oe, and after that, the magnetic moment was measured as a function of temperature increase. This gave the field-cooled (FC) curve. The magnetic behavior of samples versus applied magnetic field (M-H curves) was obtained using maximum applied fields up to 1.0 T at the temperatures of 20 K and 300 K.

The annotations of samples and experimental parameters as well as the results of phase analyses are given in Table 1.

Table 1 Annotations of samples, γ-irradiation doses and dose rates, sample isolation procedure, percentage of Fe(II) in isolated solid samples, percentage of Fe^{2+} in HCl acidified solution of dissolved samples and phase analysis determined using XRD, ED and/or Mössbauer spectroscopy.

Samples / Reference	Dose / kGy	Dose rate / kGy h^{-1}	Washing with ethanol	Admixing glycerol	Dissolution with conc. HCl	Fe(II) in isolated solid samples* / %	Fe^{2+} by $KMnO_4$ titrations** / %	Phase analysis***
S0	-	-	✓	-	-	-	-	Amorphous ("$Fe(OH)_3$")
S1	36	~7	✓	-	-	17.3	-	$Fe_{2.83}O_4$
S2	130	~7	✓	-	-	0.0	-	δ-FeOOH (major phase) + α-FeOOH (minor impurity)
S3	36	~31	-	-	-	10.0	-	$Fe_{2.75}O_4$ (major phase) + γ-Fe_2O_3 (minor phase)
$S3_{HCl}$	36	~31	-		✓		67.7	-
$S3_{Gly}$	36	~31	-	✓	✓	9.9	-	Phase F + $Fe(OH)_2$ + GR(CO_3^{2-}) + α-FeOOH
S4	130	~31	-	-	-	-	-	δ-FeOOH (major phase) + α-FeOOH (minor impurity)
$S4_{HCl}$	130	~31	-	-	-	-	96.1	-
$S4_{Gly}$	130	~31	-	✓	-	86.0	-	$Fe(OH)_2$ + GR(CO_3^{2-}) + $C_{13}H_{10}ClNO$

*Relative amount of Fe(II) determined by Mössbauer spectroscopy (sample $S3_{Gly}$ and $S4_{Gly}$) or by measuring XRD lattice parameters (samples S1 and S3). ** Relative amount of Fe^{2+} determined by $KMnO_4$ titration upon acidification and dissolution of γ-irradiated samples. ***XRD, Electron diffraction (ED) and Mössbauer results.

3. Results and discussion

Fig. 1 shows XRD powder patterns of samples S1 to S4 with admixed silicon (Si) as an internal standard for precise unit cell parameters calculations. The XRD patterns of sample S1 and S3 revealed the presence of substoichiometric magnetite. Stoichiometric magnetite Fe_3O_4 (card no. 19-0629, space group Fd-3m) has an inverse spinel structure with O^{2-} forming a face-centered cubic lattice and iron cations occupying interstitial sites. Ideally, stoichiometric magnetite ($^{Tet}Fe^{III}[^{Oct}Fe^{II}Fe^{III}]O_4$) has the ferrous to ferric ratio $Fe^{II}/Fe^{III} = 0.5$, *i.e.* 33.3 % of total iron in stoichiometric magnetite is present as Fe^{II}. Maghemite (γ-Fe_2O_3, card no. 39-1346, space group $P4_132$) can be regarded as fully oxidized magnetite. In maghemite, oxygen vacancies form in the crystal structure to account for charge balance. Therefore, the substoichiometric magnetite $Fe_{3-x}O_4$ has stoichiometry between Fe_3O_4 and γ-Fe_2O_3. Accordingly, x can range from zero in stoichiometric magnetite to 1/3 in completely oxidized magnetite ($Fe_{2.67}O_4$). The oxidation of Fe^{II} to Fe^{III} is accompanied by a linear decrease of lattice cell parameter of stoichiometric magnetite from a = 8.396 Å to a = 8.349 Å in maghemite. The calculated lattice cell parameters of samples S1 and S3 are a = 8.365 Å and a = 8.354 Å, which correspond to the stoichiometries of $Fe_{2.83}O_4$ and $Fe_{2.75}O_4$, respectively (Table 2) [38].

The XRD patterns of samples S2 and S4 perfectly matched the patterns of feroxyhyte (card no. 77-0247). A small quantity of goethite (card no. 20-0713) was present in both samples as an impurity. This is in line with the fact that feroxyhyte has never appeared as a single phase [23]. The XRD patterns of non-irradiated sample S0 that was obtained by isolation of precipitate from the $FeCl_3$ alkali aqueous solution prior the γ-irradiation is given in the Supplementary Material (Fig. S1).

The results of line broadening analyses are given in Table 3. The volume-averaged domain size (D_v) of the dominant crystalline phase of samples S1 to S4 was determined using Le Bail refinements (program GSAS). The D_v values of substoichiometric magnetite were 6.4 and 7.5 nm for samples S1 and S3, respectively. In case of sample S2 and S4, D_v values were estimated at 16.4 and 11.8 nm, whereas the estimated D_v values in the direction of the c-axis were ~ 6.4 and 5.6 nm, respectively. These crystal anisotropies are in accordance with anisotropic disc-like (higher anisotropy) and roll-like (lower anisotropy) morphologies of sample S2 and S4, respectively (Fig. 3 and 5).

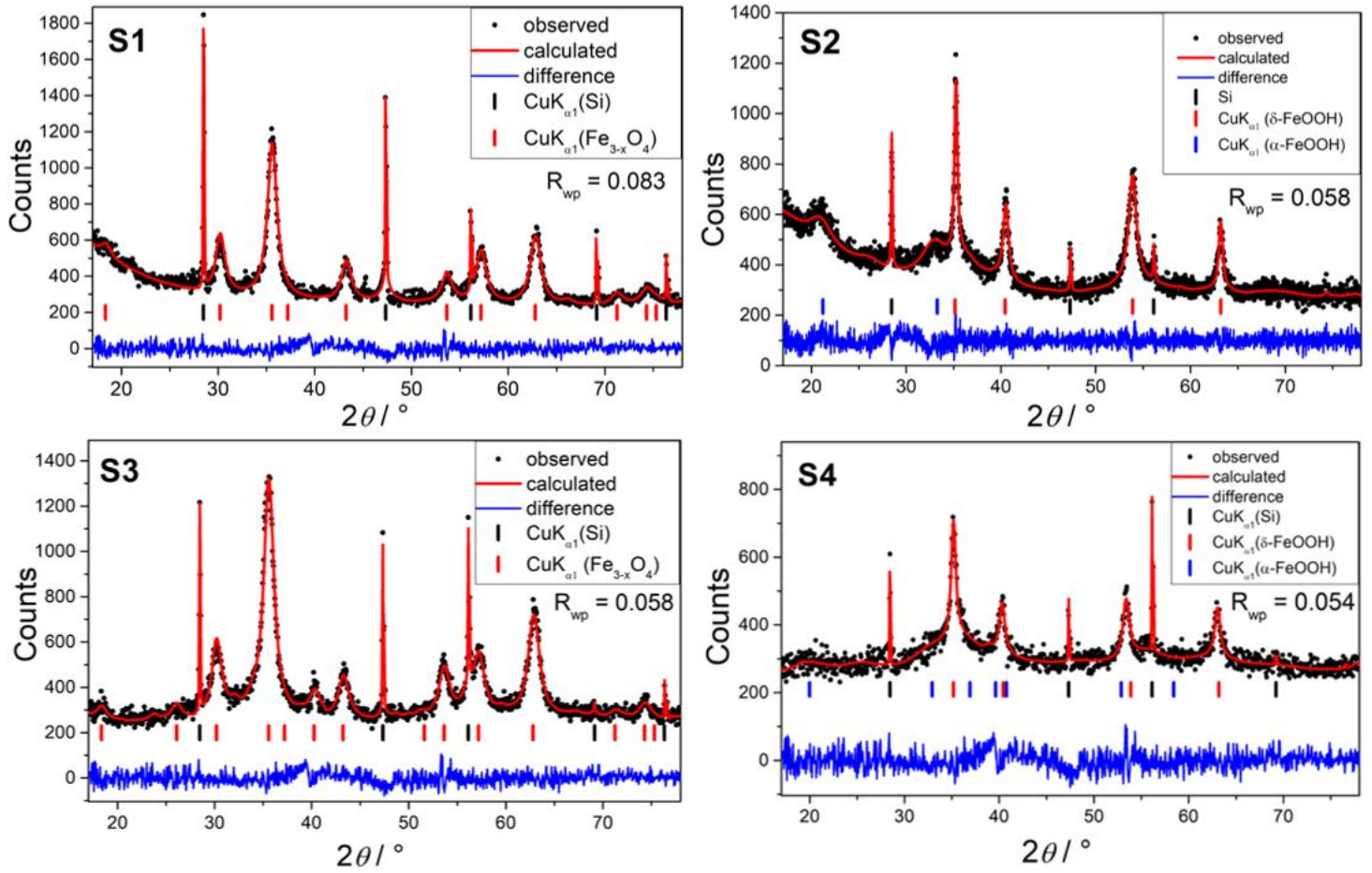

Fig. 1 XRD powder patterns of samples S1 to S4 with admixed silicon (Si) as an internal standard for precise unit cell parameters measurement.

Table 2 XRD major phases, space group, lattice parameters, and stoichiometry for samples S1 to S4 as well as corresponding ICDD cards.

Sample	**Major XRD phase (mineral name)**	**Space group**	**Lattice parameters**	**Stoichiometry**
S1	Fe_3O_4 (Magnetite)	$Fd\bar{3}m$	a = 8.365 Å V = 585.33 Å^3	$^{Tet}Fe^{III}[^{Oct}Fe^{II}_{0.49}Fe^{III}_{1.34}\square_{0.17}]O_4$ $Fe_{2.83}O_4$
S2	δ-FeOOH (Feroxyhyte)	$P\bar{3}m1$	a = 2.942(1) Å c = 4.573(3) Å V = 34.28 Å^3	$Fe^{III}OOH$
S3	Fe_3O_4 (Magnetite)	$Fd\bar{3}m$	a = 8.354 Å V = 583.02 Å^3	$^{Tet}Fe^{III}[^{Oct}Fe^{II}_{0.25}Fe^{III}_{1.5}\square_{0.25}]O_4$ $Fe_{2.75}O_4$
S4	δ-FeOOH (Feroxyhyte)	$P\bar{3}m1$	a = 2.948(1) Å c = 4.635(4) Å V =34.88 Å^3	$Fe^{III}OOH$
$S3_{gly}$	Phase F	$P4_132$	a = 8.3953(5) Å V = 591.7(1) Å^3	γ-$Fe_2^{III}O_3$ or $Fe^{III}[Fe^{II}Fe^{III}]O_4$
	$Fe(OH)_2$ (Iron(II) hydroxide)	$P\bar{3}m1$	a = 3.259(1) Å c = 4.629(2) Å V = 42.6 (1) Å^3	$Fe^{II}(OH)_2$

$S4_{gly}$	$Fe(OH)_2$ (Iron(II) hydroxide)	$P\bar{3}m1$		$Fe^{II}(OH)_2$
ICDD card number	**Reference ICDD phase (mineral name)**	**Space group**	**Lattice parameters**	**Stoichiometry**
19-0629	Fe_3O_4 (Magnetite)	$Fd\bar{3}m$	a = 8.3960 Å V = 591.86 Å^3	$^{Tet}Fe^{III}_{1.00}[^{Oct}Fe^{II}_{1.00}Fe^{III}_{1.00}\square_{0.00}]O_4$ Fe_3O_4
39-1346	γ-Fe_2O_3 (Maghemite)	$P4_132$	a = 8.3515 Å V = 582.50 Å^3	$^{Tet}Fe^{III}_{1.00}[^{Oct}Fe^{II}_{0.00}Fe^{III}_{1.67}\square_{0.33}]O_4$ $Fe_{2.67}O_4$ or Fe_2O_3
13-0089	$Fe(OH)_2$ (Iron(II) hydroxide)	$P\bar{3}m1$	a = 3.2580 Å c = 4.6050 Å V = 42.33 Å^3	$Fe^{II}(OH)_2$
77-0247	δ-FeOOH (Feroxyhyte)	$P\bar{3}m1$	a =2.95000 Å c = 4.56000 Å V = 34.30 Å^3	$Fe^{III}OOH$
46-0098	$Fe_6(OH)_{12}(CO_3)$ (Green Rust)	$R\bar{3}m$	a = 3.1691 Å c = 22.5620 Å V = 196.24 Å^3	$Fe^{II}_4Fe^{III}_2(OH)_{12}CO_3 \cdot 3H_2O$

22-1618	N-(p-Chlorophenyl) benzamide $C_{13}H_{10}ClNO$			

*The stoichiometry of substoichiometric magnetite $Fe_{3-x}O_4$ is calculated by formula $^{Tet}Fe^{3+}[^{Oct}Fe^{2+}_{1-3x}Fe^{3+}_{1+2x}\square_x]O_4$ [38]

Table 3 The volume-averaged domain size (D_v) of the dominant crystalline phase of samples S1 to S4 as determined from the results of Le Bail refinements (program GSAS). In the case of feroxyhyte (sample S2 and S4), the diffraction lines indicate the presence of size anisotropy with smaller D_v value in the direction parallel to *c*-axis.

Sample	Phase	The volume-averaged domain size (D_v) of the dominant crystalline phase (Le Bail refinement (GSAS software))	
		D_v / nm	$D_v \parallel c$-axis / nm
S1	Magnetite	6.4	-
S2	Feroxyhyte	16.4	6.4
S3	Magnetite	7.5	-
S4	Feroxyhyte	11.8	5.6

Fig. 2 shows electron microscopy analysis of sample S1. TEM micrograph shows spherical nanoparticles of 4.7 nm in size (a). HRTEM micrograph shows lattice fringes typical for the spinel-type structure (b). The inset shows SAED (selected area electron diffraction) powder patterns indexed to Fe_3O_4 (magnetite). The annular bright field (ABF) micrograph of sample S1 shows the dark and bright spots that correspond to heavy (iron) and light (oxygen) atoms, respectively (c). The high-angle annular dark field (HAADF) micrographs of one magnetite nanoparticle oriented in [110] zone show clearly visible periodic bright spots (d). Fig. 2e shows a simulated model of the magnetite structure in [110] zone that corresponds to the labeled area (brown atoms are Fe and red are oxygen). The experimentally observed bright spots in the HAADF image (d) perfectly match the positions of Fe atoms in the simulated model of the magnetite structure (e). The presence of maghemite is excluded because the diffraction lines at high d-values are missing (Fig S3 in the Supplementary Material.).

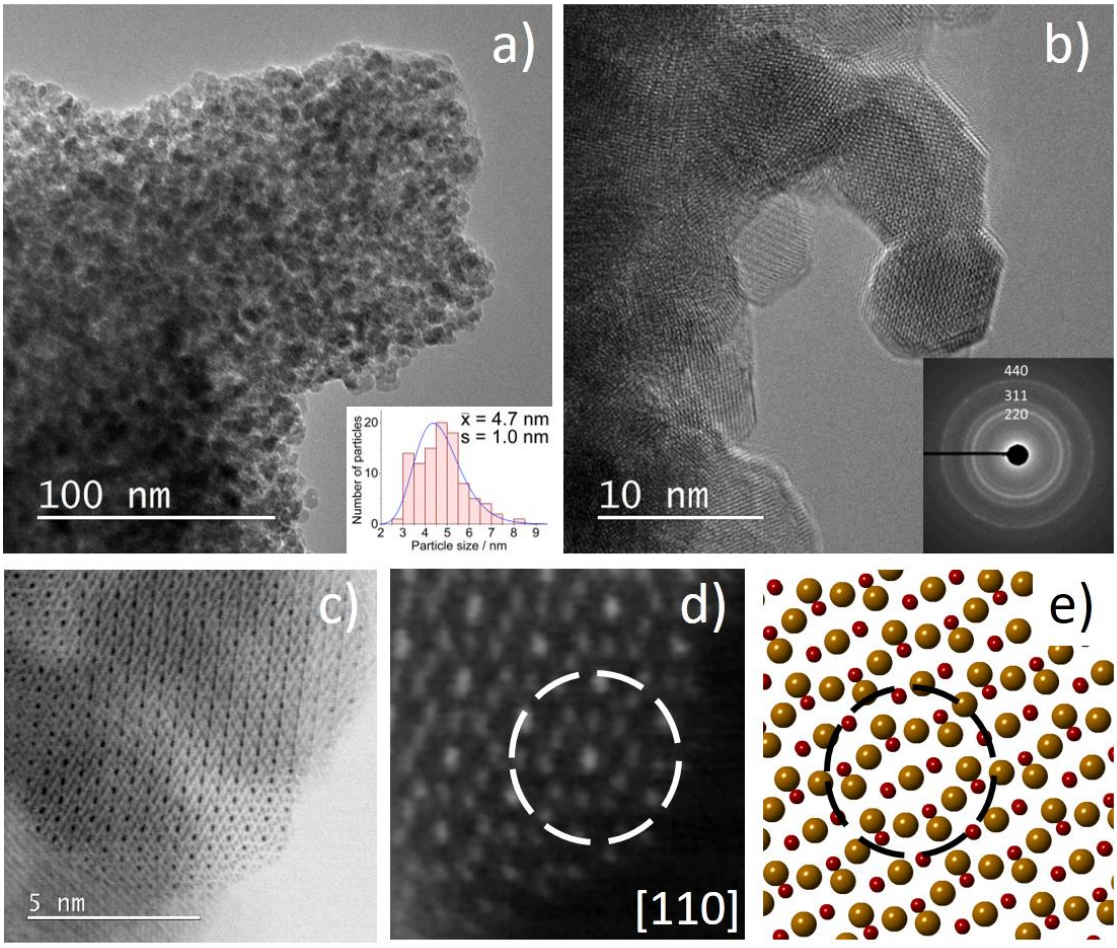

Fig. 2 TEM image of sample S1 (a). The particle size distribution is shown in the inset. HRTEM image with SAED (selected area electron diffraction) in the inset (b). The powder patterns are indexed to Fe_3O_4 (magnetite). ABF (annular bright field) micrograph of sample S1 (c); HAADF (high-angle annular dark field) micrographs of one magnetite nanoparticle oriented in [110] zone (d). The model of the magnetite structure in [110] zone (brown atoms are Fe and red are oxygen) (e).

Fig. 3 shows the results of SEM and TEM analyses. Fig. 3a shows the SEM image of sample S2. The nanodisc-like morphology is visible. The diffuse and coarse appearance of nanodiscs suggests the hydrated surfaces. Fig. 3b shows the TEM bright-field micrograph of sample S2 (b). The coarse nanodiscs and darker rod-like morphologies are visible (b). The electron powder diffraction patterns correspond well to δ-FeOOH (c). Importantly, the darker rod-like shapes are indeed the same δ-FeOOH nanodiscs oriented approximately perpendicular to the rest of the horizontally placed nanodiscs (d). The changes of size and thickness due to the different nanorods-electron beam orientations confirmed this hypothesis. From HRTEM image (e) and FFT (Fast Fourier Transform) in the inset, it was found that nanodiscs are oriented in the [0001] direction. The nanodiscs grow on the basal plane in the direction of the *c*-axis (c) that coincides with the simulated diffraction patterns (e). The thickness of an individual thin nanodisc is about 2.2 nm (f), which corresponds roughly to five unit cells.

Fig. 4 shows TEM micrographs of sample S3 with HAADF image of spherical magnetite NPs (inset at the top) and particle size distribution (inset at the bottom). The TEM image of sample S3 (another detail) shows that sample S3 is not homogeneous and that contains spherical and rod-like NPs (b). The inset (bottom right) shows a rod-like, very elongated rectangle NP (b). The SAED powder patterns of spherical NPs were indexed as Fe_3O_4 (magnetite) (c), whereas the one rod-like NP (d), several rod-like NPs (e) and a bunt of rod-like NPs (f) were indexed as maghemite (γ-Fe_2O_3). The rod-like NPs do not consist of feroxyhyte and/or magnetite as it is shown in Fig. S4 in the Supplementary Materials.

Fig. 5a shows TEM bright-field micrograph of rod-like NPs (sample S4). Fig. 5b shows TEM dark-field micrograph of rod-like NPs at higher magnification. An enlarged detail showing the rolled-up nature of rod NPs (c). Fig. 5d shows HAADF image with FFT (inset) of δ-FeOOH rod-like nanoparticle having the diffraction patterns with streaks, characteristic of tubular structures, similar to that of a multi-walled carbon nanotube [39]. The zone is again [0001]. The powder electron diffraction patterns are indexed as δ-FeOOH (e). A characteristic intensity profile over the "crumpled" foil (f). The thicker parts have a higher intensity than the thinner ones, which confirms the tubular (hollow) morphology of δ-FeOOH rod-like NPs. The tubular morphology can be formed by curling of uniformly very thin platelets due to their high surface tension.

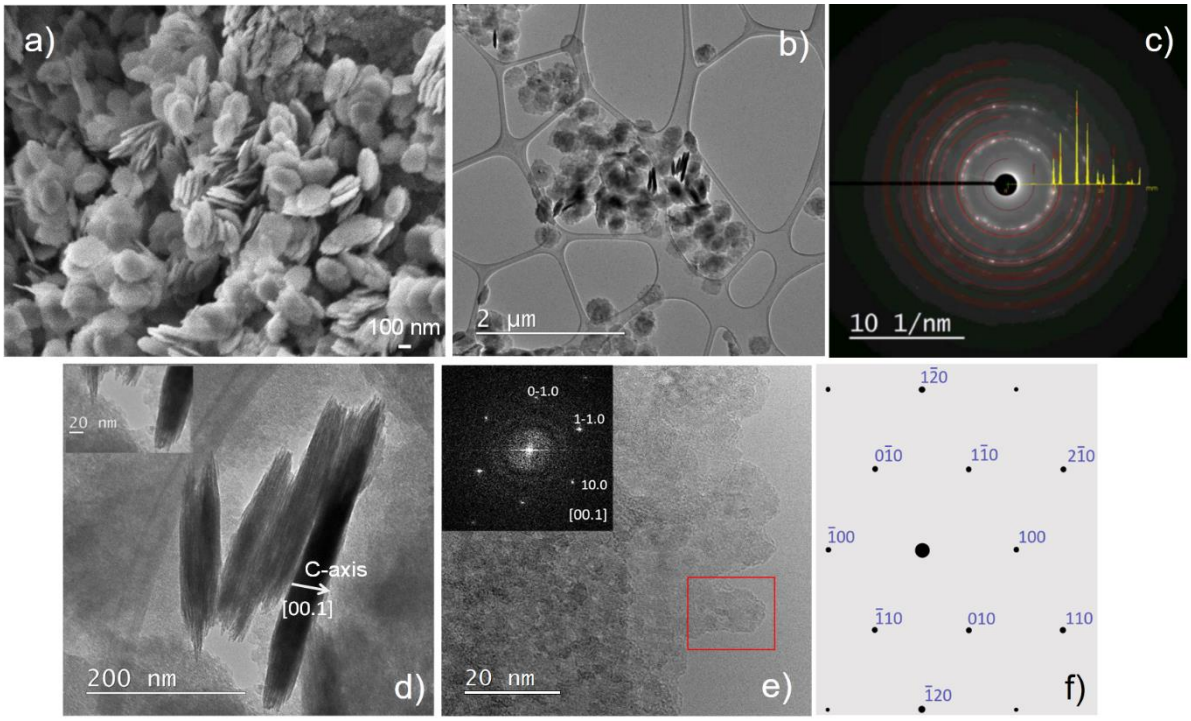

Fig. 3 The SEM image of sample S2 showing diffuse and coarse nanodisc-like morphologies (a). The TEM bright-field micrograph of sample S1 (b). The nanodiscs and darker rod-like morphologies were visible (b). The electron powder diffraction patterns correspond well to the δ-FeOOH (c). The darker rod-like shapes are nanodiscs that grow on the basal plane in the direction of the *c*-axis (d). The thickness of an individual thin nanodisc is about 2.2 nm (inset), whereas the full thickness of the discs is about 40 nm. The HRTEM image (e) and FFT (inset) show that nanodiscs are oriented in [0001] direction (c), which coincides with the simulated diffraction patterns (f).

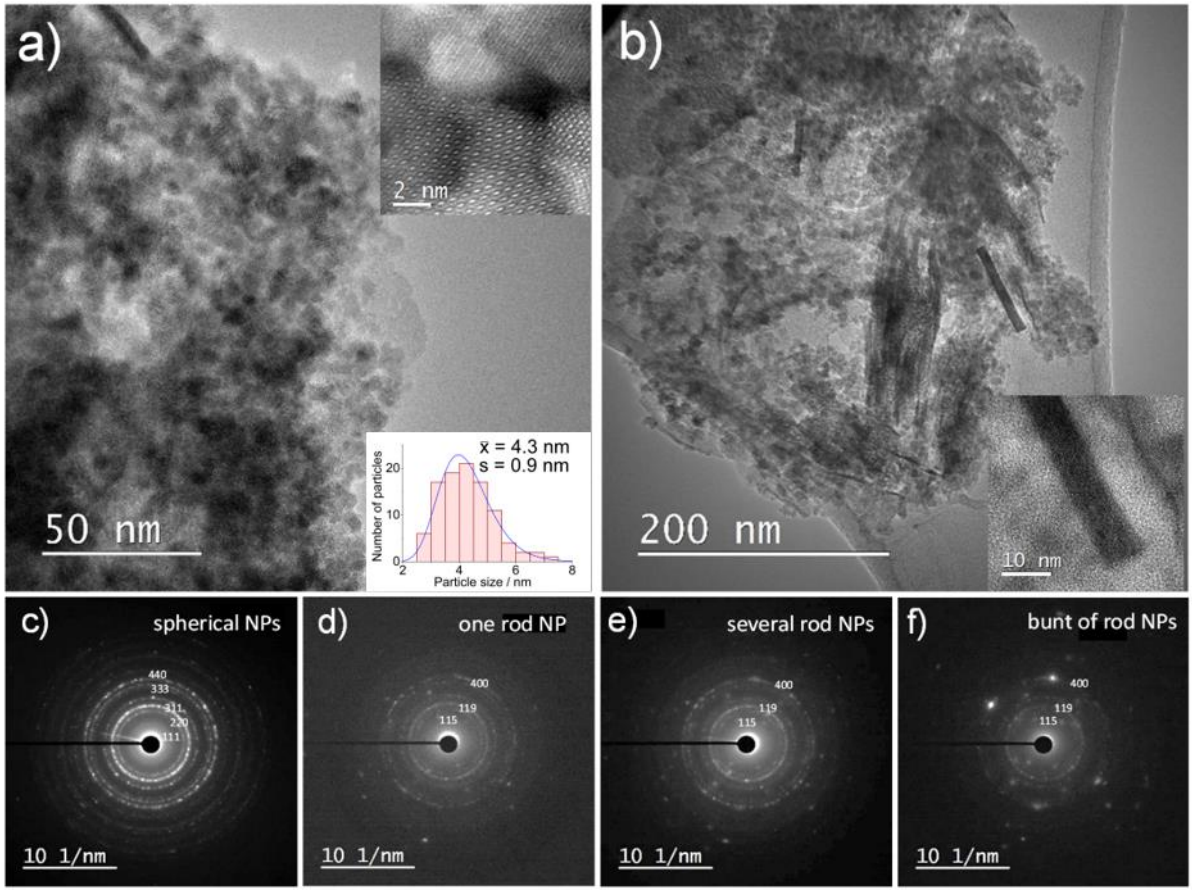

Fig. 4 TEM micrographs of sample S3 with HAADF image of magnetite NPs (inset at the top) and particle size distribution (inset at the bottom) (a); TEM image of sample S3 (another detail) showing spherical and rod-like NPs (b), the inset (bottom right) shows rod-like, very elongated rectangle NP (b); SAED of spherical NPs indexed as Fe_3O_4 (magnetite) (c); SAED of one rod-like NP indexed as maghemite (γ-Fe_2O_3) (d); SAED of several rod-like NPs indexed to γ-Fe_2O_3 (e); SAED of rod-like bunt indexed to γ-Fe_2O_3 (f).

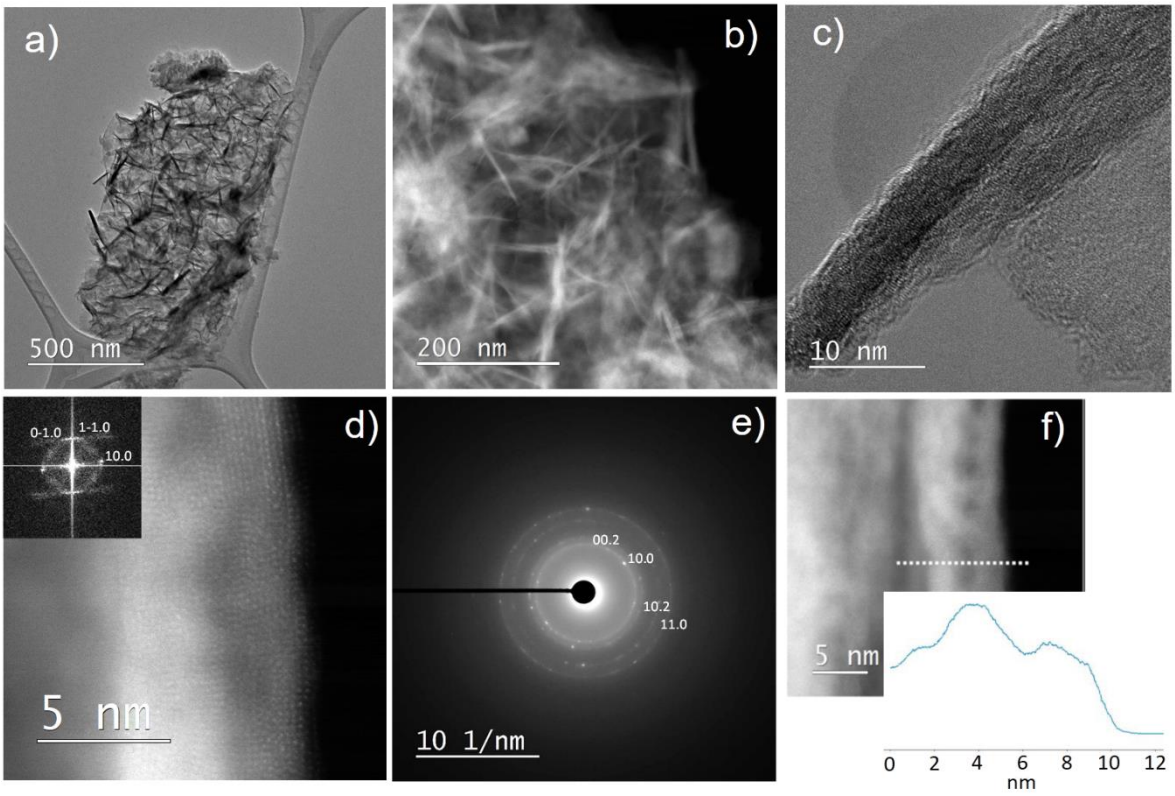

Fig. 5 TEM bright-field micrograph of sample S4 showing rod-like NPs (a). TEM dark-field micrograph showing rod-like NPs at higher magnification (b). Enlarged detail of sample S4 showing rolled-up nature of rod-like NPs (c). HAADF image with FFT (inset) of δ-FeOOH rod-like NP having the diffraction patterns with streaks characteristic for tubular morphologies (d). The powder electron diffraction patterns are indexed as δ-FeOOH (e). A characteristic intensity profile over the "crumpled" foil (f). The thicker parts have a higher intensity than the thinner ones.

Fig. 6 shows the room-temperature Mössbauer spectra of samples S1 to S4. The Mössbauer spectrum of sample S1 is characterized by a collapsing sextet M_D with broadened lines and unusual shapes because of the small particle size and complex magnetic and interparticle interactions [14]. The M_D sextet is fitted to the distribution of hyperfine magnetic fields. The Mössbauer spectra of samples S2, S3, and S4 are characterized with a superposition of a doublet and a sextet. The doublet D1 is due to the presence of high spin Fe(III) in a superparamagnetic state (SP doublet). In accordance with the XRD and HRTEM results, the sextet M_D is assigned to δ-FeOOH NPs (sample S2 and S4) and the sextet M_D to substoichiometric magnetite and maghemite NPs (sample S3). The particle size has a strong influence on the Mössbauer parameters, because of the magnetically ordered materials in the form of very small particles (about 5-10 nm in size) exhibit superparamagnetic behavior [40,41]. Superparamagnetic nanoparticles show doublets in the Mössbauer spectrum at room

temperature [42]. In the presence of small and large magnetic nanoparticles, the room-temperature Mössbauer spectra consist of a superposition of doublets and sextets [3]. In the present case, due to the similar Mössbauer room-temperature parameters of substoichiometric magnetite and δ-FeOOH NPs the magnetic phases were assigned in line with XRD, HRTEM, and magnetic results. The Mössbauer parameters are summarized in Table 4.

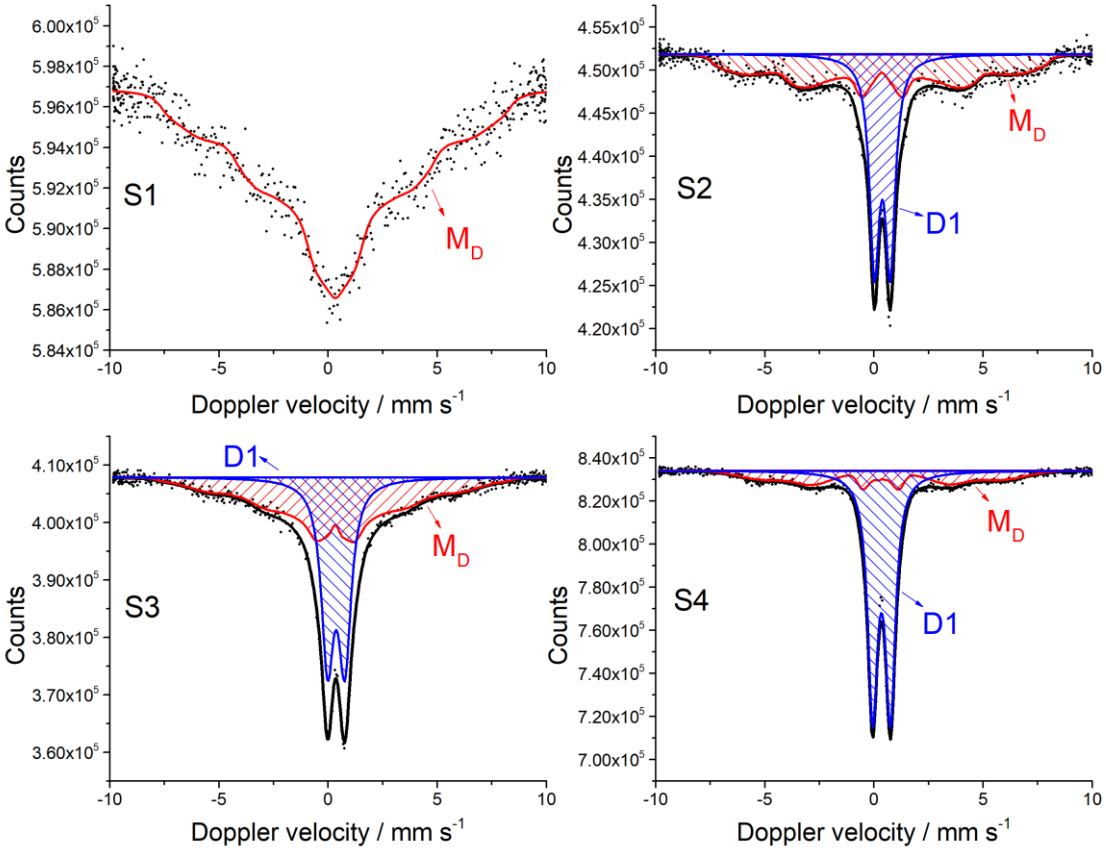

Fig. 6 The room-temperature Mössbauer spectra of samples S1 to S4.

Table 4 ^{57}Fe Mössbauer parameters at 20 °C calculated for selected samples.

Sample	Fitting curve	δ / mm s^{-1}	Δ or 2ε / mm s^{-1}	B_{hf} / T	Γ / mm s^{-1}	Relative area (%)	Fe(II) / %	χ^2
S1	M_D	0.33	0.04	23.14	0.79	100		1.06
S2	D1	0.38	0.72		0.54	46.2		1.24
	M_D	0.33	-0.07	29.57	0.41	53.8		
S3	D1	0.37	0.79		0.69	45.5		1.10
	M_D	0.30	-0.05	21.83	0.40	54.5		
S4	D1	0.35	0.82		0.54	73.5		2.84
	M_D	0.35	0.09	28.83	0.18	26.5		
$S3_{gly}$	R	0.36			5.10	67.3	9.9	1.00
	D1	0.30	0.68		0.52	22.8		
	D3	1.06	2.84		0.49	9.9		
$S4_{gly}$	D1	0.41	0.49		0.70	14.0	86.0	1.10
	D2	1.02	2.20		0.70	17.2		
	D3	1.14	2.87		0.54	68.8		

Key: δ = isomer shift given relative to α-Fe at RT; Δ = quadrupole splitting; 2ε = quadrupole shift; B_{hf} = hyperfine magnetic field; Γ = line width. Error: $\delta = \pm 0.01$ mm s^{-1}; $\Delta = \pm 0.01$ mm s^{-1}; $B_{hf} = \pm 0.2$ T; χ^2 = goodness of fitting (1.00 - relatively very good fitting; 2.00 - relatively good fitting).

Fig. 7 shows the zero-field-cooled (ZFC) and field-cooled (FC) magnetization of samples S0 to S4 as a function of temperature at a magnetic field strength of H = 100 Oe. The maximum temperature in the ZFC curve (T_{max}) is related to the blocking temperature (T_B). Above the blocking temperature, the magnetic moments flip and reverse their direction frequently enough to produce in average zero magnetization, which is characteristic of superparamagnetic particles. As each particle with a given volume is determined by its corresponding T_B value, a wide or narrow distribution of particle volumes will produce a T_B distribution and will also result in a broad or narrow maximum in the ZFC curve. Furthermore, the temperature at which the ZFC and FC curves merge, T_{irr}, corresponds to the magnetic moment deblocking of the largest particle in the sample. At temperatures higher than T_{irr} all the particles show superparamagnetic behavior. The closeness of T_{max} and T_{irr} indicates a sharp distribution of the blocking temperatures.

The ZFC curve of non-irradiated sample S0 is characterized by low magnetization and sharp maximum at T_{max} = 50 K. At temperatures above T_{max}, the ZFC and FC curve virtually completely overlap, however, the careful inspection shows that they merge at T_{irr} = 90 K. The sharp ZFC maximum and closeness of T_{max} and T_{irr} indicates a narrow particle size distribution.

Sample S1 (substoichiometric magnetite, $Fe_{2.83}O_4$) shows ambiguous magnetic properties. The closeness of T_{max} at 120 K and T_{irr} at 150 K suggests a narrow particle size distribution, which is in line with TEM results (Fig. 2), however, the flattening of the ZFC curve below the T_{irr} and its wide-ranging maximum around 120 K suggests the broad distribution of blocking temperatures. Actually, the broad ZFC maximum can be explained by magnetic frustration induced by interparticle interactions and surface and finite size effects [43,44] such as substitution of magnetic cations by vacancies, the presence of dangling and broken bonds, surface spin canting and disorder, anisotropic dipole-dipole interactions and the random distribution of easy axis [45–51].

Sample S3 is characterized with moderately broad ZFC maximum at T_{max} = 120 K and T_{irr} at 278 K. The large distance of T_{irr} and T_{max} indicates a broad particle size distribution, which agrees with TEM results (Fig. 4) that show two types of particle morphologies in sample S3 (long rods and small spherical nanoparticles). The mixture of two very different morphologies contributes to the broad particle size distributions.

The ZFC-FC curves of δ-FeOOH, samples S2 (nanodiscs) and S4 (tubular rod-like) show a remarkable difference in magnetic behavior in comparison to ZFC-FC curves of samples S1 and S3. The ZFC and FC curves of samples S2 and S4 show irreversible behavior and high divergence up to 300 K regardless of the morphology of the particles, which confirms the exceptional intrinsic room-temperature magnetic properties of δ-FeOOH with the Curie temperature of both samples above 300 K.

Fig. 8 shows the near room-temperature (300 K, open symbols) and low-temperature (20 K, filled symbols) magnetization behaviour of samples S0 to S4 as a function of the applied magnetic field up to 1.0 T. At 300 K sample S0 shows a linear dependence of magnetization with the applied magnetic field, which is in agreement with the paramagnetic behavior. On the other hand, the hysteresis loop slightly opens at 20 K, which might be due to uncompensated surface spins at the boundary of the crystalline domains. Samples S1 to S4 show superparamagnetic behavior (zero coercivity fields and no remanent magnetization) with reversible S-shaped magnetization at 300 K. In superparamagnetic particles, all magnetic moments fluctuate with the relaxation time being shorter than the measuring time, and that is why coercivity equals zero [52]. The time scale of magnetization measurements is about ~10^2

s, whereas the time scale of Mössbauer spectroscopy is ~10^{-9} s. Samples synthesized at a lower dose (sample S1 versus S3 and sample S2 versus S4) rate exhibit higher magnetization values. At 20 K, samples S1, S2, and S3 preserve the superparamagnetic behavior, whereas the sample S4 shows an unsaturated weak hysteresis loop, therefore indicating the presence of the blocked magnetic particles with a coercivity of H_c = 308 Oe and remanence of M_R = 0.64 emu g^{-1}.

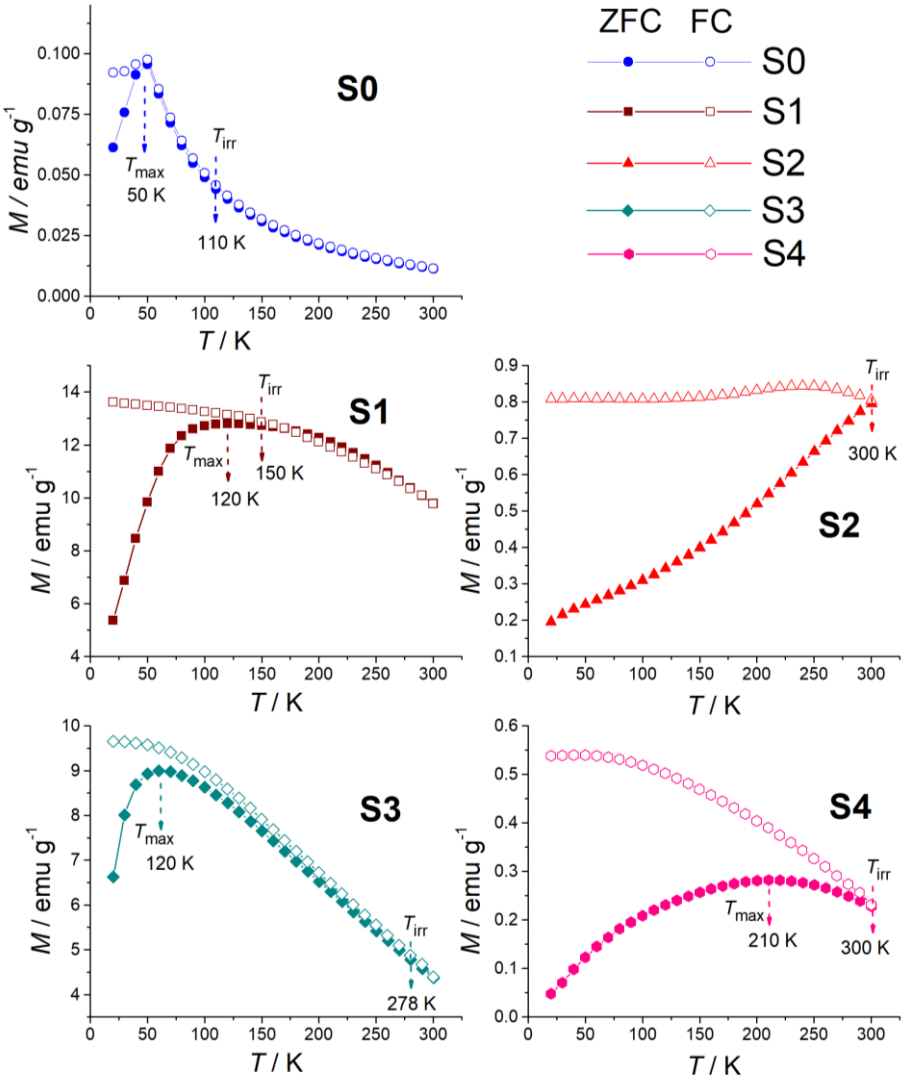

Fig. 7 The Zero-field-cooled (ZFC, empty symbols) and field-cooled (FC, filled symbols) magnetization of samples S0 to S4 as a function of temperature at a magnetic field strength of B = 100 Oe (10 mT).

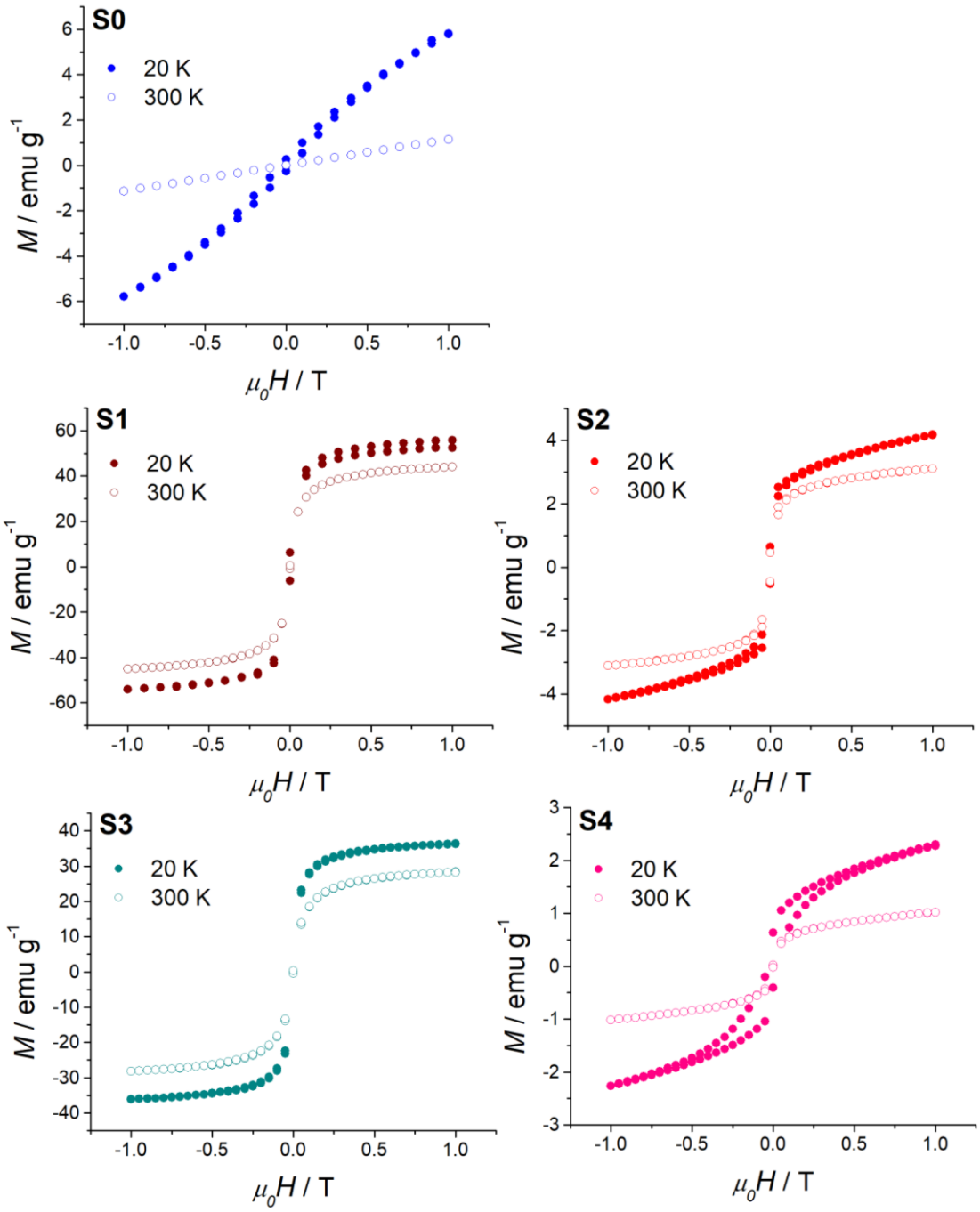

Fig. 8 The near room-temperature (T = 300 K, empty symbols) and low-temperature (T = 20 K, filled symbols) magnetization behavior of samples S0 to S4 as a function of the applied magnetic field up to 1.0 T.

In this work, iron(III) chloride aqueous colloidal solutions (pH ≅ 9) in the presence of 2-propanol and amino-dextran (DEAE dextran) were deoxygenated by nitrogen and then γ-irradiated at doses of 36 and 130 kGy. The addition of 2-propanol and bubbling with nitrogen gas highlighted the reducing conditions upon γ-irradiation [11,12,53–56] and one would

expect the reduction of Fe(III) precursor to Fe(II)-products. However, the conventional isolated samples contained virtually no Fe(II) (Table 2). For instance, the samples S1 and S3 that were γ-irradiated at a dose of 36 kGy contained 17 % and 10 % of Fe(II), respectively (Table 1 and 2). The samples γ-irradiated at a higher dose of 130 kGy for which one would expect a much higher quantity of Fe(II) did not contain Fe(II) at all. Therefore, in order to ascertain the formation of Fe(II) intermediate products prior to their oxidation during the conventional process of isolation, the samples were isolated by admixing glycerol [14]. Glycerol chemisorbs to the oxygen sensitive nanoparticles and then, the glycerol hydroxy groups easily oxidize to aldehyde or carboxylic acid groups, which lower the probability of oxygen reaching and oxidizing the structural low-valence metal cations such as Fe(II) [14,57].

Fig. 9 shows the XRD powder patterns (a, c) and Mössbauer spectra (b, d) of samples $S3_{Gly}$ (a, b) and $S4_{Gly}$ (c, d) that were isolated by admixing glycerol. The XRD patterns of sample $S3_{Gly}$ (Table 2) match best with the patterns of iron(II) hydroxide ($Fe(OH)_2$) [58], Green Rust I ($GR(CO_3^{2-})$, ideal chemical formula $Fe^{II}_4Fe^{III}_2(OH)_{12}CO_3 \cdot 3H_2O$ [57], phase F (the most similar to γ-Fe_2O_3; however the unit cell parameters a = 8.3953(5) Å fitted the best to stoichiometric magnetite [59]) and goethite (α-FeOOH). The room-temperature Mössbauer spectrum of sample $S3_{Gly}$ consists of an inner doublet D1 due to the high spin Fe(III) and/or superparamagnetic particles and an outer doublet D3 due to Fe(II) present in $Fe(OH)_2$ and $GR(CO_3^{2-})$. The "magnetic singlet" component (symbolized with R) is introduced to improve the fitting [34]. The amount of Fe(II) in sample $S3_{Gly}$ is estimated to 9.9 % on the basis of the relative area of outer doublet D3.

The XRD powder patterns of sample $S4_{Gly}$ match best with the patterns of $Fe(OH)_2$, $GR(CO_3^{2-})$ and organic compound N-(p-Chlorophenyl) benzamide that may be a result of radiolytic degradation of DEAE-dextran. The room-temperature Mössbauer spectrum of sample $S4_{Gly}$ consists of three doublets; a doublet D1 due to the high spin Fe(III) and/or superparamagnetic particles, a doublet D2 due to Fe(II) in $GR(CO_3^{2-})$ and a doublet D3 due to Fe(II) in $Fe(OH)_2$. The amount of Fe(II) in sample $S4_{Gly}$ is estimated to 86 % on the basis of relative areas of doublets D2 and D3 (Table 3). In addition to the Mössbauer determination of Fe(II) in solid products, the concentrations of Fe^{2+} in the acidified solutions containing dissolved γ-irradiation products were determined using potassium permanganate titrations. The concentrations of Fe^{2+} in acidified solutions were 67.7 % and 96.1 % for the dose of 36 and 130 kGy, respectively. Therefore, at the dose of 130 kGy the Fe(II) values determined in the acidified solution by $KMnO_4$ titration (96.1 % of Fe^{2+}) and in solid product (admixing glycerol) by Mössbauer spectroscopy (86.0 % of Fe(II)) agreed well, however at the dose of

36 kGy there was high inconsistency between the Fe^{2+} value in the solution (67.7 %) and Fe(II) value in solid product (9.9 % determined by Mössbauer spectroscopy (Table 1). This is due to the impossibility of room temperature Mössbauer spectroscopy to determine Fe(II) in superparamagnetic nanoparticles. On the other side, the concentrations of Fe(II) and Fe^{2+} found in this work fit well with the values found in our previous work [14], where we used dextran sulfate instead of DEAE-dextran.

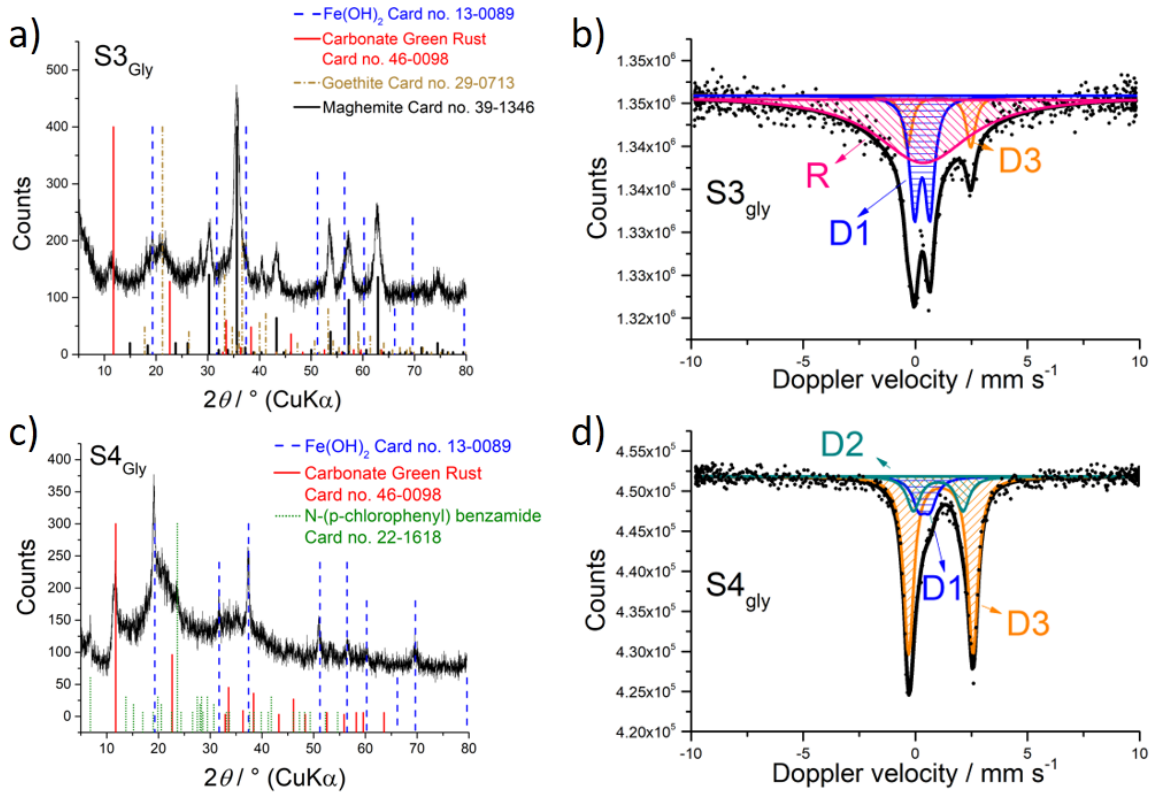

Fig. 9 XRD powder patterns (a, c) and room-temperature Mössbauer spectra (b, d) of samples $S3_{Gly}$ (a, b) and $S4_{Gly}$ (c, d).

Fig. 10 shows a simplified scheme of the transformations that proceed upon γ-irradiation of deoxygenated Fe(III) alkaline aqueous precursor in the presence of 2-propanol and DEAE-dextran. γ-irradiation in a series of reactions reductively dissolved "$Fe(OH)_3$" precursor which re-precipitated as $Fe_{3-x}O_4$ at a dose of 36 kGy or as $Fe(OH)_2$ at a dose of 130 kGy. However, after the septum has been removed and the γ-irradiated suspensions have come into contact with air the Fe(II)-products readily oxidized. The degree of oxidation is

proportional to the relative amount of radiolytically formed Fe(II), from which it follows that there is an optimal concentration of Fe(II) for obtaining magnetite nanoparticles. This conclusion is in line with our previous work, where the substoichiometric magnetite nanoparticles were synthesized using γ-irradiation of microemulsions [53] or Fe(III) alkaline aqueous precursor in the presence of dextran sulfate [14]. However, at a dose of 130 kGy when almost 100 % of $Fe(OH)_2$ was radiolytically formed, the highly reactive $Fe(OH)_2$ topotactically oxidized to $GR(CO_3^{2-})$ after coming in contact with oxygen and CO_2 from the air, and further to δ-FeOOH without any structural changes. The lower dose rate (~7 kGy h^{-1}) favors the δ-FeOOH layered nanodisc morphology, whereas the higher dose rate (~31 kGy h^{-1}) favors the formation of tubular rod-like δ-FeOOH nanoparticles.

Fig. 10 The simplified scheme of the transformations that proceeded upon γ-irradiation.

4. Conclusions

The substoichiometric $Fe_{3-x}O_4$ nanoparticles ~ 5 nm in size and layered δ-FeOOH nanodiscs and tubular rod-like δ-FeOOH nanoparticles were synthesized by γ-irradiation of iron(III) chloride deaerated alkaline aqueous colloidal solutions in the presence of 2-propanol and DEAE-dextran. It was shown that γ-irradiation generated strong reducing conditions that radiolytically reduced "$Fe(OH)_3$" up to $Fe(OH)_2$, which then after coming in contact with oxygen and CO_2 from air topotactically oxidized to $GR(CO_3^{2-})$ and further to δ-FeOOH without any structural changes. The lower dose rate (~7 kGy h^{-1}) favors the δ-FeOOH layered nanodisc morphology, whereas the higher dose rate (~31 kGy h^{-1}) favors the formation of

tubular rod-like δ-FeOOH nanoparticles. The layered nanostructured δ-FeOOH discs have a diameter of ~256 nm and thickness of ~40 nm and each disc is comprised of approximately eighteen laterally stacked thin nanodiscs of about 2.2 nm in size. The ZFC and FC curves of δ-FeOOH samples show irreversible behavior and high divergence up to 300 K regardless of the morphology of the particles, which confirms the exceptional intrinsic room-temperature magnetic properties of δ-FeOOH with the Curie temperature of both samples above 300 K.

Acknowledgments

This work was financially supported by the Croatian Science Foundation under the project UIP-2017-05-7337 "The impact of polymers on the radiolytic synthesis of magnetic nanoparticles" (POLRADNANOP). Financial support from the Slovenian Research Agency, the research program P2-0393 (Goran Dražić) is acknowledged. Marijan Gotić and Goran Štefanić acknowledge the "Croatian science foundation under project 2634 and by the QuantixLie center of excellence, a project co-financed by the Croatian government and the European Union through the European regional development fund – the competitiveness and cohesion operational programme (KK.01.1.1.01)."

Author contributions

Ivan Marić performed the synthesis of the samples and participated in the preparation of figures and the manuscript, participated in the characterization of samples, performed the determination of Fe(II) and critically read the manuscript, Goran Dražić performed and analyzed transmission electron microscopy of the samples, Goran Štefanić analyzed XRD measurements, Krešo Zadro performed SQUID measurements, Marijan Gotić measured and analyzed Mössbauer spectra, contributed to the design of the research and participated in the preparation of the manuscript, Tanja Jurkin designed and conducted the research, performed the synthesis of the samples and participated in the preparation of the manuscript.

Data availability

The raw/processed data required to reproduce these findings cannot be shared at this time due to technical or time limitations.

References

[1] R.A. Revia, M. Zhang, Magnetite nanoparticles for cancer diagnosis, treatment, and treatment monitoring: Recent advances, Mater. Today. 19 (2016) 157–168. doi:10.1016/j.mattod.2015.08.022.

[2] M. Sharon, G. Oza, A. Gupta, S. Pandey, Super-paramagnetic iron oxide nanoparticles (spions) as nano-flotillas for hyperthermia: A paradigm for cancer theranostics, Adv. Nanomater. Synth. Prop. Appl. (2014) 307–328. doi:10.1201/b16966.

[3] M. Gotić, S. Musić, Mössbauer, FT-IR and FE SEM investigation of iron oxides precipitated from $FeSO_4$ solutions, J. Mol. Struct. 834–836 (2007) 445–453. doi:10.1016/j.molstruc.2006.10.059.

[4] S. Ivanković, M. Gotić, M. Jurin, S. Musić, Photokilling squamous carcinoma cells SCCVII with ultrafine particles of selected metal oxides, J. Sol-Gel Sci. Technol. 27 (2003) 225–233. doi:10.1023/A:1023715004575.

[5] J.-P. Jolivet, C. Chanéac, E. Tronc, Iron oxide chemistry. From molecular clusters to extended solid networks, Chem. Commun. (2004) 477–483. doi:10.1039/b304532n.

[6] M. Gotić, S. Musić, Synthesis of nanocrystalline iron oxide particles in the iron(III) acetate/alcohol/acetic acid system, Eur. J. Inorg. Chem. (2008). doi:10.1002/ejic.200700986.

[7] E.B. Gracien, Z. Ruimin, X. LiHui, L.K. Kanza, I. Lopaka, Effects of pH on the morphology of iron oxides synthesized under gamma-irradiation, J. Radioanal. Nucl. Chem. 270 (2006) 473–478. doi:10.1007/s10967-006-0374-4.

[8] S. Wang, H. Xin, The γ-irradiation-induced chemical change from β-FeOOH to Fe_3O_4, Radiat. Phys. Chem. 56 (1999) 567–572. doi:10.1016/S0969-806X(99)00319-9.

[9] J. Du, H. Liu, Preparation of superparamagnetic γ-Fe_2O_3 nanoparticles in nonaqueous medium by γ-irradiation, J. Magn. Magn. Mater. 302 (2006) 263–266. doi:10.1016/j.jmmm.2005.09.016.

[10] P. Brunetti, Z. Wang, W. Lu, L. Spinu, J. Fang, K. Sunderland, Synthesis of γ-Fe_2O_3/polypyrrole nanocomposite materials, Mater. Lett. 58 (2004) 3136–3140. doi:10.1016/j.matlet.2004.05.055.

[11] M. Gotić, T. Jurkin, S. Musić, From iron(III) precursor to magnetite and vice versa, Mater. Res. Bull. 44 (2009) 2014–2021. doi:10.1016/j.materresbull.2009.06.002.

[12] T. Jurkin, M. Gotić, G. Štefanić, I. Pucić, Gamma-irradiation synthesis of iron oxide nanoparticles in the presence of PEO, PVP or CTAB, Radiat. Phys. Chem. 124 (2016) 75–83. doi:10.1016/j.radphyschem.2015.11.019.

[13] L. Mikac, M. Ivanda, M. Gotić, T. Mihelj, L. Horvat, Synthesis and characterization of silver colloidal nanoparticles with different coatings for SERS application, J. Nanoparticle Res. 16 (2014) 1–13. doi:10.1007/s11051-014-2748-9.

[14] I. Marić, G. Štefanić, M. Gotić, T. Jurkin, The impact of dextran sulfate on the radiolytic synthesis of magnetic iron oxide nanoparticles, J. Mol. Struct. 1183 (2019) 126–136. doi:10.1016/j.molstruc.2019.01.075.

[15] T. Jurkin, G. Štefanić, G. Dražić, M. Gotić, Synthesis route to δ-FeOOH nanodiscs,

Mater. Lett. 173 (2016) 55–59. doi:https://doi.org/10.1016/j.matlet.2016.03.009.

[16] J.M. Bigham, U. Schwertmann, L. Carlson, E. Murad, A poorly crystallized oxyhydroxysulfate of iron formed by bacterial oxidation of Fe(II) in acid mine waters, Geochim. Cosmochim. Acta. 54 (1990) 2743–2758. doi:10.1016/0016-7037(90)90009-A.

[17] R.M. Cornell, U. Schwertmann, The iron oxides: structure, properties, reactions, occurrences and uses: second ed., 2003. doi:10.1002/3527602097.

[18] C.B. Koch, C.A. Oxborrow, S. Mørup, M.B. Madsen, A.J. Quinn, J.M.D. Coey, Magnetic properties of feroxyhyte (δ-FeOOH), Phys. Chem. Miner. 22 (1995) 333–341. doi:10.1007/BF00202774.

[19] M. Bo Madsen, S. Mørup, C.J.W. Koch, O.K. Borggaard, A study of microcrystals of synthetic feroxyhite (δ′FeOOH), Surf. Sci. 156 (1985) 328–334. doi:10.1016/0039-6028(85)90591-6.

[20] R.J. Pollard, Q.A. Pankhurst, Ferrimagnetism in fine feroxyhite particles, J. Magn. Magn. Mater. 99 (1991) L39–L44. doi:10.1016/0304-8853(91)90045-C.

[21] M. Pernet, X. Obradors, J. Fontcuberta, J.C. Joubert, J. Tejada, Magnetic structure and supermagnetic properties of δ-FeOOH, IEEE Trans. Magn. 20 (1984) 1524–1526. doi:10.1109/TMAG.1984.1063311.

[22] M.C. Pereira, E.M. Garcia, A. Cândido da Silva, E. Lorençon, J.D. Ardisson, E. Murad, J.D. Fabris, T. Matencio, T. de Castro Ramalho, M.V.J. Rocha, Nanostructured δ-FeOOH: a novel photocatalyst for water splitting, J. Mater. Chem. 21 (2011) 10280. doi:10.1039/c1jm11736j.

[23] M. Sestu, D. Carta, M.F. Casula, A. Corrias, G. Navarra, Novel interpretation of the mean structure of feroxyhyte, J. Solid State Chem. 225 (2015) 256–260. doi:10.1016/j.jssc.2015.01.003.

[24] A.A. Jelle, M. Hmadeh, P.G.O. Brien, D.D. Perovic, G.A. Ozin, Photocatalytic Properties of All Four Polymorphs of Nanostructured Iron Oxyhydroxides, (2016). doi:10.1002/cnma.201600251.

[25] S. Tresintsi, K. Simeonidis, S. Estradé, C. Martinez-Boubeta, G. Vourlias, F. Pinakidou, M. Katsikini, E.C. Paloura, G. Stavropoulos, M. Mitrakas, Tetravalent Manganese Feroxyhyte: A Novel Nanoadsorbent Equally Selective for As(III) and As(V) Removal from Drinking Water, Environ. Sci. Technol. 47 (2013) 9699–9705. doi:10.1021/es4009932.

[26] I.S.X. Pinto, P.H.V.V. Pacheco, J.V. Coelho, E. Lorençon, J.D. Ardisson, J.D. Fabris, P.P. de Souza, K.W.H. Krambrock, L.C.A. Oliveira, M.C. Pereira, Nanostructured δ-FeOOH: An efficient Fenton-like catalyst for the oxidation of organics in water, Appl. Catal. B Environ. 119–120 (2012) 175–182. doi:10.1016/J.APCATB.2012.02.026.

[27] P. Chen, K. Xu, X. Li, Y. Guo, D. Zhou, J. Zhao, X. Wu, C. Wu, Y. Xie, Ultrathin nanosheets of feroxyhyte: A new two-dimensional material with robust ferromagnetic behavior, Chem. Sci. 5 (2014) 2251–2255. doi:10.1039/c3sc53303d.

[28] P. Chagas, A.C. Da Silva, E.C. Passamani, J.D. Ardisson, L.C.A. De Oliveira, J.D. Fabris, R.M. Paniago, D.S. Monteiro, M.C. Pereira, δ-FeOOH: A superparamagnetic

material for controlled heat release under AC magnetic field, J. Nanoparticle Res. 15 (2013). doi:10.1007/s11051-013-1544-2.

[29] P. Martins, A. Larrea, R. Gonçalves, G. Botelho, E. V. Ramana, S.K. Mendiratta, V. Sebastian, S. Lanceros-Mendez, Novel anisotropic magnetoelectric effect on δ-FeO(OH)/P(VDF-TrFE) multiferroic composites, ACS Appl. Mater. Interfaces. 7 (2015) 11224–11229. doi:10.1021/acsami.5b01196.

[30] B. Liu, Y. Wang, H.-Q. Peng, R. Yang, Z. Jiang, X. Zhou, C.-S. Lee, H. Zhao, W. Zhang, Iron Vacancies Induced Bifunctionality in Ultrathin Feroxyhyte Nanosheets for Overall Water Splitting, Adv. Mater. 30 (2018) 1803144. doi:10.1002/adma.201803144.

[31] M. Gotić, S. Popović, S. Musić, Formation and characterization of δ-FeOOH, Mater. Lett. 21 (1994) 289–295. doi:10.1016/0167-577X(94)90192-9.

[32] A.A. Olowe, Y. Marie, P. Refait, J.M.R. Génin, Mechanism of formation of delta FeOOH in a basic aqueous medium, Hyperfine Interact. 93 (1994) 1783–1788. doi:10.1007/BF02072946.

[33] A.Y. Polyakov, A.E. Goldt, T.A. Sorkina, I. V. Perminova, D.A. Pankratov, E.A. Goodilin, Y.D. Tretyakov, Constrained growth of anisotropic magnetic δ-FeOOH nanoparticles in the presence of humic substances, CrystEngComm. 14 (2012) 8097–8102. doi:10.1039/c2ce25886b.

[34] N. Nishida, S. Amagasa, Y. Kobayashi, Y. Yamada, Synthesis of superparamagnetic δ-FeOOH nanoparticles by a chemical method, Appl. Surf. Sci. 387 (2016) 996–1001. doi:10.1016/j.apsusc.2016.06.179.

[35] B.H. Toby, R.B. Von Dreele, GSAS-II : the genesis of a modern open-source all purpose crystallography software package, J. Appl. Crystallogr. 46 (2013) 544–549. doi:10.1107/S0021889813003531.

[36] A. Le Bail, Whole powder pattern decomposition methods and applications: A retrospection, Powder Diffr. 20 (2005) 316–326. doi:10.1154/1.2135315.

[37] D. Pajić, K. Zadro, R.E. Vanderberghe, I. Nedkov, Superparamagnetic relaxation in $Cu_xFe_{3-x}O_4$ (x = 0.5 and x = 1) nanoparticles, J. Magn. Magn. Mater. 281 (2004) 353–363. doi:10.1016/j.jmmm.2004.04.126.

[38] C.A. Gorski, M.M. Scherer, Determination of nanoparticulate magnetite stoichiometry by Mossbauer spectroscopy, acidic dissolution, and powder X-ray diffraction: A critical review, Am. Mineral. 95 (2010) 1017–1026. doi:10.2138/am.2010.3435.

[39] A.A. Lucas, P. Lambin, Diffraction by DNA, carbon nanotubes and other helical nanostructures, Reports Prog. Phys. 68 (2005) 1181–1249. doi:10.1088/0034-4885/68/5/R05.

[40] S. Mørup, Mössbauer effect in small particles, Hyperfine Interact. 60 (1990) 959–973. doi:10.1007/BF02399910.

[41] S. Kamali-M., T. Ericsson, R. Wäppling, Characterization of iron oxide nanoparticles by Mössbauer spectroscopy, Thin Solid Films. 515 (2006) 721–723. doi:10.1016/j.tsf.2005.12.180.

[42] M. Mikhaylova, D.K. Kim, N. Bobrysheva, M. Osmolowsky, V. Semenov, T.

Tsakalakos, M. Muhammed, Superparamagnetism of Magnetite Nanoparticles: Dependence on Surface Modification, Langmuir. 20 (2004) 2472–2477. doi:10.1021/la035648e.

[43] E. Lima, A.L. Brandl, A.D. Arelaro, G.F. Goya, Spin disorder and magnetic anisotropy in Fe_3O_4 nanoparticles, J. Appl. Phys. 99 (2006). doi:10.1063/1.2191471.

[44] G. Muscas, G. Concas, S. Laureti, A.M. Testa, R. Mathieu, J.A. De Toro, C. Cannas, A. Musinu, M.A. Novak, C. Sangregorio, S.S. Lee, D. Peddis, The interplay between single particle anisotropy and interparticle interactions in ensembles of magnetic nanoparticles, Phys. Chem. Chem. Phys. 20 (2018) 28634–28643. doi:10.1039/c8cp03934h.

[45] E. Brok, C. Frandsen, D.E. Madsen, H. Jacobsen, J.O. Birk, K. Lefmann, J. Bendix, K.S. Pedersen, C.B. Boothroyd, A.A. Berhe, G.G. Simeoni, S. Mørup, Magnetic properties of ultra-small goethite nanoparticles, J. Phys. D. Appl. Phys. 47 (2014). doi:10.1088/0022-3727/47/36/365003.

[46] C. Carbone, F. Di Benedetto, P. Marescotti, C. Sangregorio, L. Sorace, N. Lima, M. Romanelli, G. Lucchetti, C. Cipriani, Natural Fe-oxide and -oxyhydroxide nanoparticles: An EPR and SQUID investigation, Mineral. Petrol. 85 (2005) 19–32. doi:10.1007/s00710-005-0098-0.

[47] A.J. Barker, B. Cage, S. Russek, C.R. Stoldt, Ripening during magnetite nanoparticle synthesis: Resulting interfacial defects and magnetic properties, J. Appl. Phys. 98 (2005). doi:10.1063/1.2058191.

[48] J.M. Vargas, W.C. Nunes, L.M. Socolovsky, M. Knobel, D. Zanchet, Effect of dipolar interaction observed in iron-based nanoparticles, Phys. Rev. B - Condens. Matter Mater. Phys. 72 (2005) 2–7. doi:10.1103/PhysRevB.72.184428.

[49] T.J. Daou, S. Begin-Colin, J.M. Grenèche, F. Thomas, A. Derory, P. Bernhardt, P. Legaré, G. Pourroy, Phosphate Adsorption Properties of Magnetite-Based Nanoparticles, Chem. Mater. 19 (2007) 4494–4505. doi:10.1021/cm071046v.

[50] T.J. Daou, J.M. Grenèche, G. Pourroy, S. Buathong, A. Derory, C. Ulhaq-Bouillet, B. Donnio, D. Guillon, S. Begin-Colin, Coupling Agent Effect on Magnetic Properties of Functionalized Magnetite-Based Nanoparticles, Chem. Mater. 20 (2008) 5869–5875. doi:10.1021/cm801405n.

[51] T.J. Daou, G. Pourroy, J.M. Greneche, A. Bertin, D. Felder-Flesch, S. Begin-Colin, Water soluble dendronized iron oxide nanoparticles, Dalt. Trans. (2009) 4442. doi:10.1039/b823187g.

[52] K. Lipert, J. Kazmierczak, I. Pelech, U. Narkiewicz, a Slawska-Waniewska, H.K. Lachowicz, Magnetic properties of cementite (Fe_3C) nanoparticle agglomerates in a carbon matrix, Mater. Sci. 25 (2007) 399–404.

[53] M. Gotić, T. Jurkin, S. Musić, Factors that may influence the micro-emulsion synthesis of nanosize magnetite particles, Colloid Polym. Sci. 285 (2007) 793–800. doi:10.1007/s00396-006-1624-2.

[54] N. Hanžić, T. Jurkin, A. Maksimović, M. Gotić, The synthesis of gold nanoparticles by a citrate-radiolytical method, Radiat. Phys. Chem. 106 (2015) 77–82. doi:10.1016/J.RADPHYSCHEM.2014.07.006.

[55] T. Jurkin, M. Gulliš, G. Dražić, M. Gotić, Synthesis of gold nanoparticles under highly oxidizing conditions, Gold Bull. 49 (2016) 21–33. doi:10.1007/s13404-016-0179-3.

[56] T. Jurkin, K. Zadro, M. Gotić, S. Musić, Investigation of solid phase upon γ-irradiation of ferrihydrite-ethanol suspension, Radiat. Phys. Chem. 80 (2011) 792–798. doi:10.1016/j.radphyschem.2011.02.031.

[57] H.C.B. Hansen, Composition, stabilization, and light absorption of Fe(II)Fe(III) hydroxy-carbonate (‘green rust’), Clay Miner. 24 (1989) 663–669. doi:10.1180/claymin.1989.024.4.08.

[58] J.D. Bernal, D.R. Dasgupta, A.L. Mackay, The Oxides and Hydroxides of Iron and Their Structural Inter-Relationships, Clay Miner. 4 (1959) 15–30. doi:10.1180/claymin.1959.004.21.02.

[59] J.E. Jørgensen, L. Mosegaard, L.E. Thomsen, T.R. Jensen, J.C. Hanson, Formation of γ-Fe_2O_3 nanoparticles and vacancy ordering: An in situ X-ray powder diffraction study, J. Solid State Chem. 180 (2007) 180–185. doi:10.1016/j.jssc.2006.09.033.

Supplementary materials

Microstructural characterization of radiolytically synthesized feroxyhyte and magnetite nanoparticles

Ivan Marić[1], Goran Dražić[2], Goran Štefanić[3,4], Krešo Zadro[5], Marijan Gotić[3,4,*], Tanja Jurkin[1,*]

[1]*Radiation Chemistry and Dosimetry Laboratory, Ruđer Bošković Institute, 10000 Zagreb, Croatia*
[2]*Department of Materials Chemistry, National Institute of Chemistry, Hajdrihova 19, SI-1001 Ljubljana, Slovenia*
[3]*Center of Excellence for Advanced Materials and Sensing Devices, Ruđer Bošković Institute, 10000 Zagreb, Croatia*
[4]*Laboratory for Molecular Physics and Synthesis of New Materials, Division of Materials Physics, Ruđer Bošković Institute, 10000 Zagreb, Croatia*
[5]*Physics Department, Faculty of Science, University of Zagreb, Bijenička c. 32, HR-10000 Zagreb, Croatia*

[*]Corresponding authors: Tanja Jurkin, Ruđer Bošković Institute, Bijenička 54, 10000 Zagreb, Croatia, Phone: +385 1 4571 255, *E-mail address*: tjurkin@irb.hr and Marijan Gotić, Ruđer Bošković Institute, Bijenička 54, 10000 Zagreb, Croatia, *E-mail address*: gotic@irb.hr

Table of Contents

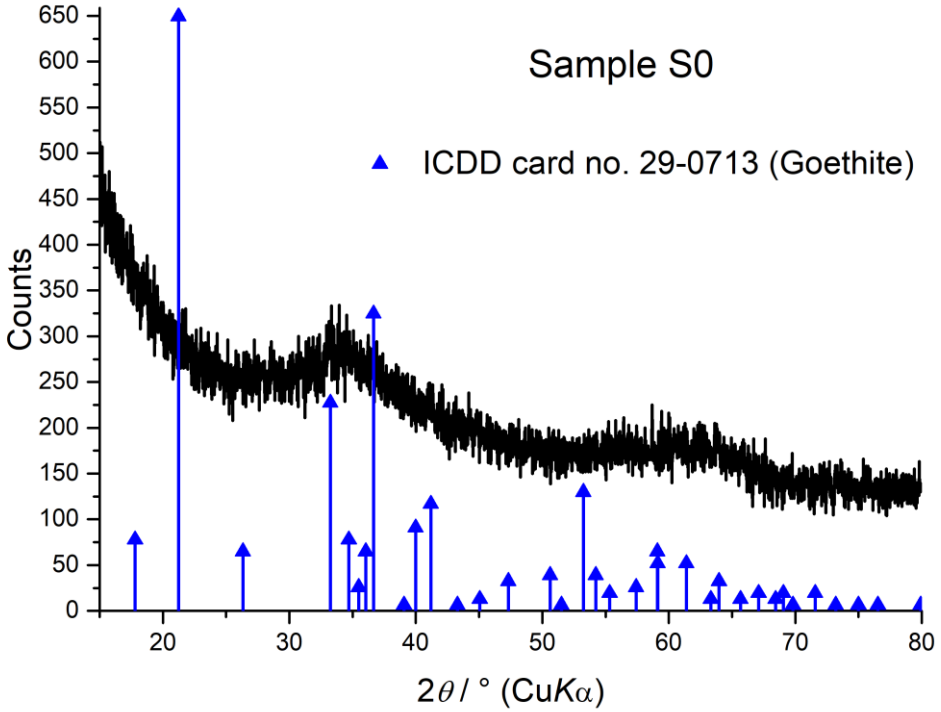

Fig. S1 XRD powder patterns of non-irradiated sample S0 obtained by isolation of precipitate from the $FeCl_3$ alkali aqueous solution prior the γ-irradiation. The sample was isolated by centrifugation, washed with ethanol and dried under vacuum at room temperature. The XRD patterns of samples S0 match the patterns of goethite (card no. 20-0713), however due to very broad maximums which reflect low crystallinity and small nanoparticle size this sample in the manuscript is regarded as "$Fe(OH)_3$".

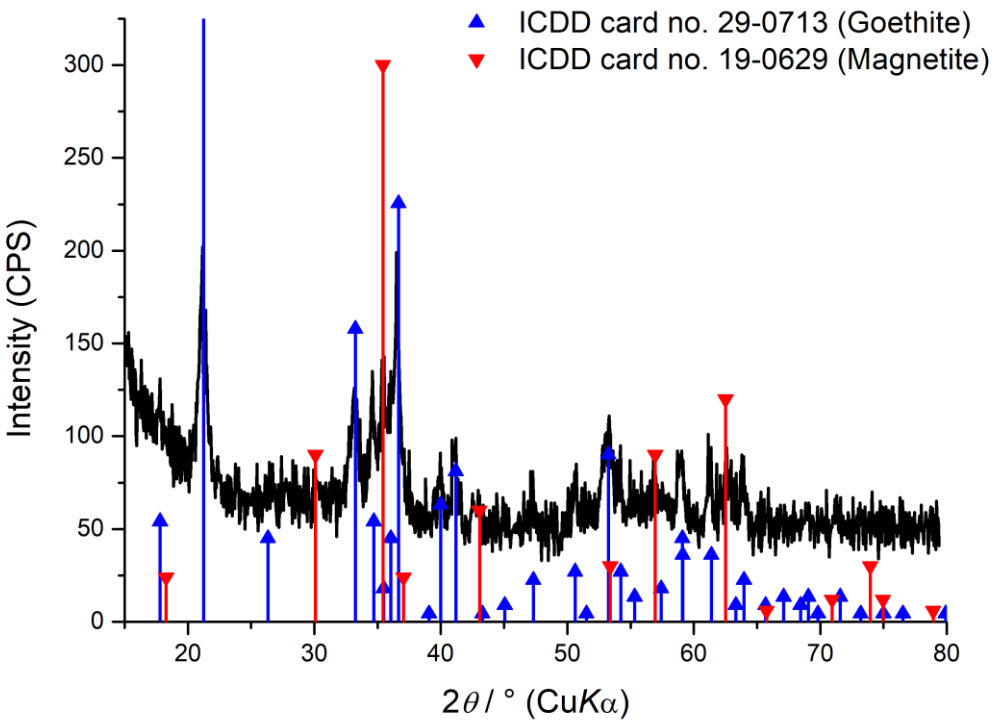

Fig. S2 XRD powder patterns of sample obtained using γ-irradiation (130 kGy), but without the addition of DEAE-dextran. The sample is mixture of goethite and magnetite.

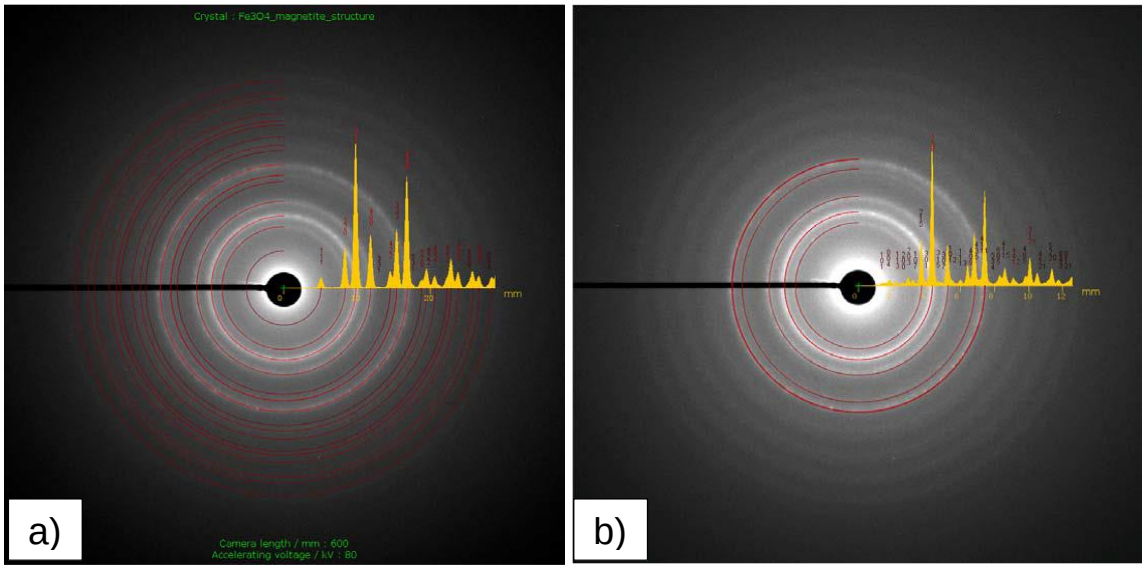

Fig S3 SAED (selected area electron diffraction) images of sample S1. The SEAD patterns correspond to magnetite (a), whereas the presence of maghemite is excluded (b), because the diffraction lines at high d-values are missed.

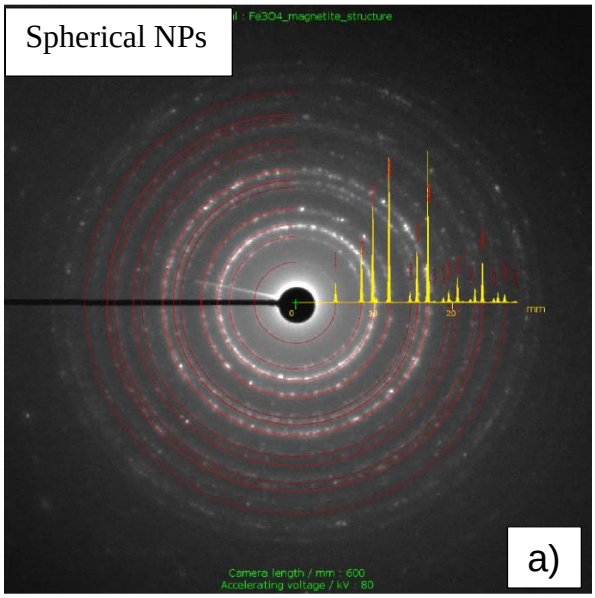
Spherical NPs
Camera length / mm : 600
Accelerating voltage / kV : 80
a)

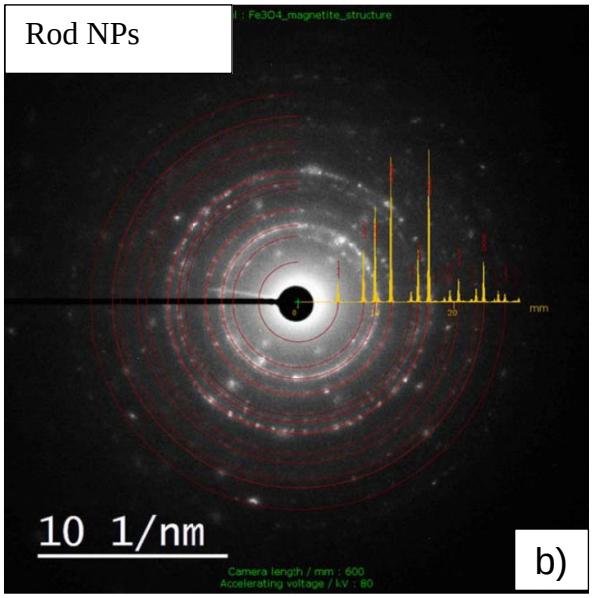
Rod NPs
10 1/nm
Camera length / mm : 600
Accelerating voltage / kV : 80
b)

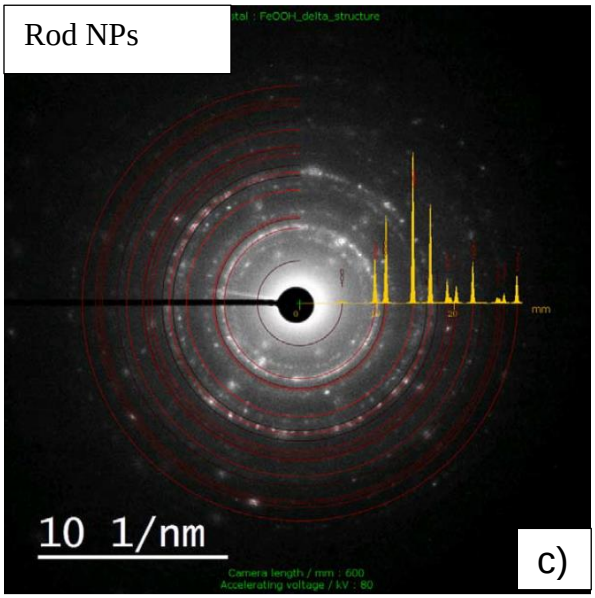
Rod NPs
10 1/nm
Camera length / mm : 600
Accelerating voltage / kV : 80
c)

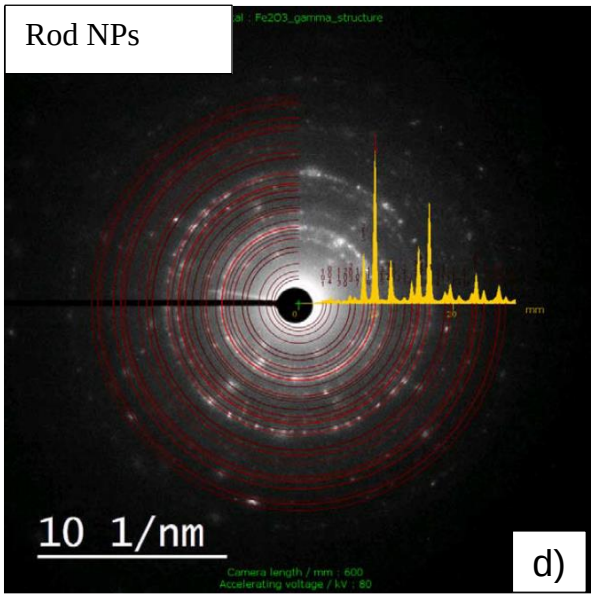
Rod NPs
10 1/nm
Camera length / mm : 600
Accelerating voltage / kV : 80
d)

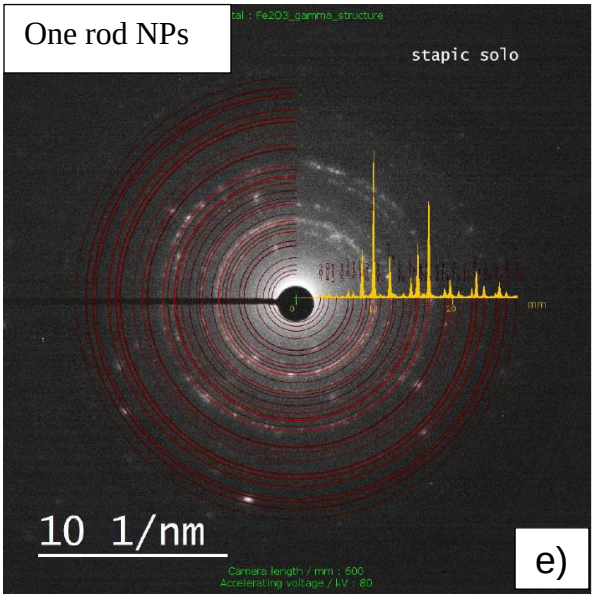
One rod NPs
stapic solo
10 1/nm
Camera length / mm : 600
Accelerating voltage / kV : 80
e)

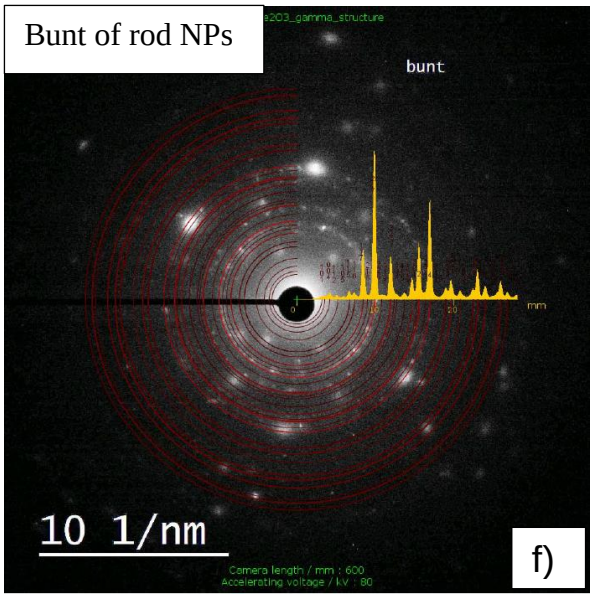
Bunt of rod NPs
bunt
10 1/nm
Camera length / mm : 600
Accelerating voltage / kV : 80
f)

Fig S4 SAED (selected area electron diffraction) images of sample S3. The SEAD patterns of spherical nanoparticles match best with magnetite (a); the rod nanoparticles – the magnetite cannot fit all SEAD patterns (b); the rod nanoparticles – the feroxyhyte cannot fit SEAD patterns (c); the rod nanoparticles – the γ-Fe_2O_3 (maghemite) fit the best SEAD patterns (d); the one rod nanoparticle – the γ-Fe_2O_3 (maghemite) fit the best SEAD patterns (e); the bunt of rod nanoparticles – the γ-Fe_2O_3 (maghemite) fit the best SEAD patterns (f).

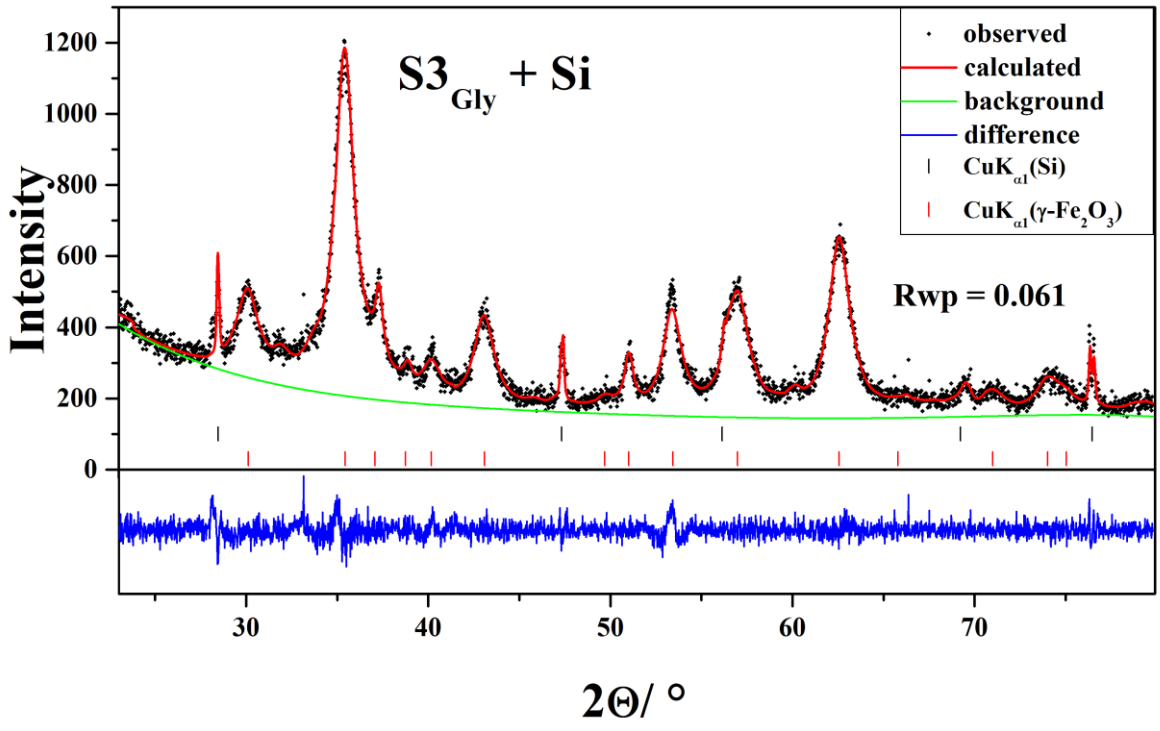

Fig. S5 XRD powder patterns of samples $S3_{Gly}$ with admixed silicon (Si) as an internal standard for precise unit cell parameters measurements. XRD patterns of sample $S3_{Gly}$ fit the best with the patterns of γ-Fe_2O_3 (maghemite). However, the calculated unit cell parameters (a = 8.3953(5) Å) match perfectly to the stoichiometric magnetite parameters (a = 8.3960 Å). Therefore, it is not clear whether this phase is magnetite or maghemite and because of that we denoted this phase as "Phase F". The possible reasons for this discrepancy lay in fact that samples $S3_{Gly}$ is mixture of several phases and maybe the two peaks at $2\Theta \cong 40^o$ do not belong to maghemite, but to some other unidentified phase.